

1 **Volcanic-tectonic structure of the Mt. Dent Oceanic Core Complex in the ultraslow**
2 **Mid-Cayman Spreading Center determined from detailed seafloor investigation**

3 **G. Haughton¹, N. W. Hayman², R. C. Searle³, Tim Le Bas⁴, and B. J. Murton⁴**

4 ¹School of Ocean and Earth Sciences, ⁴National Oceanography Center, University
5 of Southampton Waterfront Campus, European Way, Southampton, SO14 3ZH,
6 UK.

7 ²University of Texas, Institute for Geophysics, Jackson School for Geosciences,
8 10100 Burnet Rd., Austin TX, 78758, USA.

9 ³Durham University, Department of Earth Sciences. Durham, DH1 3LE, UK.

10 ⁴National Oceanography Center, European Way, Southampton, SO14 3ZH, UK.

11

12 Corresponding author: Nicholas W. Hayman (hayman@ig.utexas.edu)

13

14 **Key Points:**

- 15
- 16 • The Mid-Cayman Spreading Center is an example of how magmatism can drive cycles of ocean core
17 complex development even at ultraslow rates.
 - 18 • Decreasing detachment fault slip is marked by crosscutting higher angle faults and patterns of mass
19 wasting and sedimentation.
 - 20
 - 21 • The surface expression of hydrothermal fluid flow in vents and pockmarks is linked with the
22 mechanical evolution of oceanic core complexes.
 - 23
 - 24
 - 25

26

27 Abstract

28 The flanks of the ultraslow-spreading Mid-Cayman Spreading Center (MCSC) are characterized by
29 domal massifs, or oceanic core complexes (OCCs). The most prominent of these, Mt. Dent, comprises
30 lower-crustal and upper-mantle lithologies and hosts the Von Damm vent field (VDVF) ~12 km west of the
31 axial deep. Here-presented AUV-derived swath sonar (multibeam) mapping and deep-towed side-scan sonar
32 imagery lead to our interpretation that: (i) slip along the OCC-bounding detachment fault is ceasing, (ii) the
33 termination zone, where detachment fault meets the hanging wall, is disintegrating, (iii) the domed surface
34 of the OCC is cut by steep north-south extensional faulting, and (iv) the breakaway zone is cut by outward-
35 facing faults. The VDVF and dispersed pockmarks on the OCC's south flank further suggest that
36 hydrothermal fluid flow is pervasive within the faulted OCC. On the axial floor of the MCSC, bright
37 acoustic backscatter and multibeam bathymetry reveal: (v) a volcanic detachment hanging wall, (vi) a major
38 fault rifting the southern flank of Mt. Dent, and (vii) a young axial volcanic ridge intersecting its northern
39 flank. These observations are described by a conceptual model wherein detachment faulting and OCC
40 exhumation are ceasing during an increase in magmatic intrusion, brittle deformation, and hydrothermal
41 circulation within the OCC. Together, this high-resolution view of the MCSC provides an instructive
42 example of how OCCs formed within an overall melt-starved ultraslow spreading center can undergo
43 magmatism, hydrothermal activity, and faulting in much the same way as expected in magmatically more
44 robust slow-spreading centers elsewhere.

45

46 1. Introduction

47 Mid-ocean ridges accommodate seafloor spreading via a combination of magmatic and tectonic
48 processes (*Sykes, 1967; Cann, 1968; MacDonald & Luyendyk, 1977; Smith & Cann, 1990; Mutter &*
49 *Karson, 1992; Shaw & Lin, 1993*). Where the magmatic component of seafloor spreading is low and
50 tectonic extension is high, the oceanic basement may be characterized by large-offset detachment (normal)
51 faults that dip shallowly at the surface, yet accommodate significant seafloor spreading resulting in the
52 exhumation of lower-crustal and upper-mantle rocks at the seafloor to form oceanic core complexes (OCCs)
53 (*Karson & Dick, 1983; Cannat, 1993; Tucholke & Lin, 1994; Cann et al., 1997; Tucholke et al., 1998,*
54 *2008; Cannat et al., 2006; Ildefonse et al., 2007; Escartin et al., 2008; Schouten et al., 2010*). Indeed,
55 geodynamic modelling has found that OCCs appear to form in environments where magma, intruded into
56 the brittle lithosphere, accommodates between 30-50% of the total plate separation (*Buck et al., 2005;*
57 *Behn and Ito, 2008*).

58 Observations along the slow-spreading Mid-Atlantic Ridge (MAR), combined with geodynamic
59 modelling, suggest that OCCs evolve via a “rolling hinge”, wherein the OCC detachment fault initiates at a
60 higher angle and then, as a result of flexure and exhumation of the lower crust and/or upper mantle, is back-
61 tilted to emerge as a domal footwall (*Garces & Gee, 1997; Lavier et al., 1999; deMartin et al., 2007; Morris
62 et al., 2009*). Following this exhumation, at some point OCCs are rendered inactive and are passively
63 transported off axis. Understanding this “life cycle” (cf., *MacLeod et al., 2009*) thus hinges on
64 understanding which processes dominate the late-stage OCC evolution (e.g., *Reston et al., 2002*). *MacLeod
65 et al. (2009)* argue that for OCCs at slow spreading ridges the detachment fault migrates past the spreading
66 axis resulting in magmatic intrusion into the footwall, across the detachment fault, and into the brittle
67 hanging wall, thereby ceasing the continued exhumation of the OCC. Other models of OCC life cycles
68 envision elevated amount of magmatic intrusion to cause mechanically favorable conditions for high-angle
69 faults to cut across OCCs (*Tucholke et al., 2008; Olive et al., 2010*). But could such magmatic controls on
70 OCC development be important in ultraslow spreading centers that are thought to be generally magma-poor
71 (e.g. *Dick et al., 2003*)? Furthermore, what roles might hydrothermal activity play in OCC evolution via
72 mechanical linkages with faulting (e.g. *Hirose and Hayman, 2008*) and cooling of magmatic bodies within
73 OCCs (e.g. *Canales et al., 2017*)?

74 Here, we provide evidence that a well-developed OCC at the ultraslow-spreading Mid-Cayman
75 Spreading Center (MCSC), is in the process of “dying” as slip on the detachment faulting ceases,
76 magmatism intrudes the OCC’s footwall, and faulting accommodates extension internal to the OCC.
77 Variations in acoustic backscatter and micro-bathymetry from Autonomous Underwater Vehicle (AUV)
78 data, deep-towed side-scan sonar and shipboard multibeam data reveal the spatial and, in some cases,
79 temporal distribution of faulting across and along the OCC. We posit that this structural evolution is
80 intimately linked with magmatism and hydrothermal activity, the latter expressed at the Von Damm Vent
81 Field (*Connelly et al., 2012*). At some stage in this evolution, the OCC will then be transported off axis by
82 axial seafloor spreading, as has occurred for previous OCCs along the spreading center (*Grevemeyer et al.,
83 2018*). By documenting the structural geology observed at the surface with a range of seafloor-imaging
84 datasets, we offer a case study in the magmatic and tectonic mechanisms underlying the cessation of OCC
85 development along an ultraslow spreading-center.

86 **2. Tectonic Setting**

87 The OCC we focus on is known as Mt. Dent (*Edgar et al., 1991*) and it separates the northern and
88 southern segments of the MCSC (Figure 1). The MCSC is among the world’s deepest and slowest spreading
89 centers, having an axial depth of ~5000-7000 meters and an ultraslow full-spreading rate of ~15 mm/yr

90 (*Macdonald & Holcombe, 1978; Rosencrantz et al., 1988*). At 110 km long, the MCSC is bound by two
91 transform faults: the Oriente Fracture Zone to the north and the Swan Island Fracture Zone to the southwest.
92 The MCSC formed as a pull-apart basin between these two transform faults to accommodate Caribbean-
93 North American plate motion and retreat of the Caribbean Arc/Lesser Antilles (*LeRoy et al., 2000; Mann et*
94 *al., 2007*). Gravity analyses and seismic imaging suggest that the MCSC hosts basaltic, gabbroic, and
95 exhumed (serpentinized) mantle peridotite, and thus has been spreading by a mixture of magmatic accretion
96 and tectonic spreading for the last ~10 myr (*ten Brink et al., 2002; Grevemeyer et al., 2018*). In fact, there is
97 a clear record of ultraslow seafloor spreading dating back to at least ~20 Ma, if not ~49 Ma (*Leroy et al.,*
98 *2000; Hayman et al., 2011*).

99 As is the case for ultraslow spreading centers worldwide (*Edmonds et al., 2003; Michael et al.,*
100 *2003; Sauter et al., 2004; Tao et al., 2012*), the MCSC is well known to host basaltic and gabbroic rocks
101 along with exhumed mantle rocks (*Stroup and Fox, 1981; Hayman et al. 2011*), as well as hydrothermal
102 activity (*German et al. 2010; Connelly et al., 2012*). Yet, the deep axial depths and incompatible-element
103 enriched Mid-Ocean Ridge Basalt (MORB) compositions are indicative of some of the lowest potential
104 temperature and melt fractions of any mid-ocean ridge mantle (*Klein & Langmuir, 1987*). Similarly, seismic
105 data suggest that there is a wide range of crustal thicknesses in the Cayman Trough, with some areas hosting
106 ~3-5 km of crust, significantly thinner than crustal sections on slow-spreading centers overall, and other
107 areas comprising only exhumed mantle (*Grevemeyer et al., 2018*). Some of the thicker sections (~5 km) of
108 MCSC lower oceanic crust accreted in zones of deep partial melt and ultimately formed OCCs (*Hayman et*
109 *al., 2011; Harding et al., 2017*). Within the northern and southern areas of the axial deep, basaltic basins
110 overlie ongoing lower crustal accretion, though here too the crust is thin relative to global averages (*Van*
111 *Avendonk et al., 2017*). Lastly, peridotite samples from the MCSC are evidence of truly amagmatic seafloor
112 spreading, preserving geochemical signatures that share some similarity to Gakkal Ridge and Southwest
113 Indian Ridge mantle (*Mallick et al., 2014*). Thus, the MCSC is an overall melt-poor environment relative to
114 the global mid-ocean ridge system, though in detail there are areas of robust magmatism. Our effort here is
115 to better understand how OCCs evolve in such an environment.

116 **3. Methodology**

117 The data used here were collected during *RRS James Cook* cruises JC44 and JC81 in 2010 and 2013,
118 respectively. Shipboard swath bathymetry data, acquired using a Kongsberg-Simrad EM120 multibeam
119 sonar operating at a frequency of 10 kHz and at a speed over the ground of 2 kts, were filtered for spikes
120 and errors before being gridded at 50 m. Side-scan sonar imagery was acquired from a deep-towed 30 kHz
121 system (TOBI), that was deployed at an average altitude of ~300 m above the seafloor, and insonified the

122 axial zone of the MCSC. The data were corrected for vehicle altitude (slant-range), geographic position and
123 speed over the seafloor before being gridded at 6 m. High-resolution swath bathymetry and acoustic
124 backscatter data were acquired using a 200 kHz Kongsberg-Simrad EM2000 multibeam sonar, fitted to the
125 Autonomous Underwater Vehicle (AUV) Autosub6000 operating at an average altitude of 150 m above the
126 seafloor. Subsea navigation was provided by a combination of ultra-short baseline acoustic tracking from
127 the surface vessel, inertial navigation and Doppler velocity logging. The AUV bathymetry and acoustic
128 backscatter intensity were gridded at 1 m and the final grid position adjusted to match major features seen
129 on the GPS-navigated shipboard bathymetry maps. These data were imported into ArcGISTM and analyzed
130 using a combination of raster- and vector-based tools. Acoustic backscatter, either from TOBI side-scan
131 sonar, or AUV-derived multibeam swath sonar, is shown with light-greys as high-amplitudes and indicates
132 seafloor with high acoustic albedo. Bathymetric and backscatter images reveal a variety of morphologies
133 and textures from which features are identified (*Blondel & Murton, 1997; Searle et al., 2010*) including:
134 smooth high-reflectivity areas indicative of sheet flow lavas; smooth low-reflectivity areas indicative of soft
135 sediment cover; high-frequency, low amplitude topography with moderate to high mottled acoustic
136 reflectivity indicative of hummocky volcanic terrain, and circular or crescent-shaped features indicative of
137 volcanic edifices. The intensity of acoustic backscatter varies inversely with the thickness of pelagic
138 sediment cover.

139 Fault scarps are identified as linear or curvi-linear marking the traces of slopes in excess of 40°. Such offsets
140 in seafloor depth are in many places, but not everywhere, associated with higher intensity sonar backscatter
141 depending on sediment cover. Where appropriate, slope azimuth and inclination maps for the faults were
142 generated from 3x3 matrices applied as a high-pass filter over the gridded bathymetry data and centered on
143 each grid element. The choice of 40° slope for the fault identification probably under samples the fault
144 population and is considered here a conservative estimate. The high-resolution survey areas were
145 subsequently visually surveyed and sampled using the robotic underwater vehicle (RUV), HyBIS (*Murton et*
146 *al., 2012*) and the ROV Isis. We make reference to the ROV and RUV observations below but do not
147 present them in any detail as our focus is the regional interpretations of the bathymetric and backscatter
148 datasets.

149 **4. Results**

150 **4.1 Geology of the MCSC**

151 Based on shipboard and AUV-derived multibeam bathymetry, deep-towed side-scan sonar imagery
152 (30 kHz TOBI), and near-bottom video-surveying and sampling, we can divide the MCSC into three distinct

153 segments (Figures 1B, 2A): (1) a northern segment containing circular volcanoes and a ridge of hummocky
154 lavas that extends into the nodal deep basin marking the intersection with the Oriente Fracture Zone, (2) a
155 central segment dominated by the Mt. Dent massif, and (3) a southern segment comprising, from north to
156 south, several smooth floored basins, divided by a number of prominent NW-SE trending morphological
157 ridges and a field of hummocky and sheet-flow lavas, respectively.

158 The northern segment is dominated by a hummocky volcanic field, identified in TOBI side-scan
159 sonar records as having high acoustic backscatter and a typical mottled appearance reflecting the presence
160 of numerous small volcanic cones, as seen in other spreading centers (e.g., *Searle et al.*, 2010). This
161 hummocky volcanic field fills 85% of the width of the MCSC axial valley floor (Figure 2A, B), which is
162 itself bounded by N-S normal fault scarps (near 81°44'W and 81°50'W) forming the inner axial valley walls.
163 This field includes a number of circular volcanic edifices, up to 2.5 km in diameter, some with distinct
164 craters (Figure 2C). The center of the volcanic field contains a 9 km-long axial volcanic ridge (AVR) that
165 rises up to 600 m from the valley floor. The AVR has a series of oblique ridges trending NW and NE away
166 from its crest. One of these, on the eastern flank of the AVR, hosts an 800 m diameter volcanic pillow-lava
167 mound on top of which is the deepest (5000 m) known high-temperature hydrothermal vent field and
168 seafloor massive sulphide deposit, the Beebe Vent Field (BVF) (*Connelly et al.*, 2012), also known as the
169 Piccard Vent Field (*German et al.*, 2010; *McDermott et al.*, 2018). The BVF comprises a series of sulphide
170 mounds and black-smoker chimneys venting supercritical fluids at up to 410°C (*Webber et al.*, 2015) with
171 compositions that indicate a fluid-rock reaction zone located ~3 km below the seafloor that involves both
172 mafic and ultramafic rocks (*Webber et al.*, 2015; *McDermott et al.*, 2018). At the northern end of the AVR,
173 hummocky volcanic terrain and sheet flows cover most of the floor of the 7000 m nodal deep basin that
174 marks the junction between the MCSC and the Oriente Fracture Zone. The southern end of the AVR
175 terminates abruptly against the northern flank of Mt. Dent. Here, the AVR is at its most prominent, with the
176 crest of the AVR and its hummocky lava flanks clearly visible in the bathymetry data with bright acoustic
177 backscatter indicating it is relatively sediment free (Figure 2B).

178 Compared with the hummocky terrain of the northern segment, the southern segment of the MCSC
179 comprises several smooth-floored basins, with moderate acoustic backscatter, cut by a series of curvilinear
180 ridges and scarps (bright backscatter ribbons) that generally trend to the NW-SE (Figure 1-3). Seismic
181 imaging and sampling by dredging show these are filled with volcanic products (*Hayman et al.*, 2011; *Van*
182 *Avendonk et al.*, 2017). What we refer to here as the 'Central Basin' is divided into two oval-shaped sub-
183 basins each 8-10 km long and 3-5 km wide (Figure 3). These have flat and smooth (volcanic) seafloor and
184 the moderate intensity and homogeneous acoustic backscatter is indicative of thinly draped, sediment

185 covered lavas, likely dominated by sheet flows given the smooth surface of the seafloor (Figure 3C). We do
186 not attribute the flat nature of the seafloor in these regions to sediment blanketing over hummocky lavas
187 because such an effect is not observed elsewhere in the axial deep, the sedimentation rate is very low (*Land,*
188 1979), and the two areas are seismically interpreted to be deep volcanic basins rather than, for example,
189 flanks of an axial high.

190 The two sub-basins are separated by an obliquely trending, steep-sided, curvilinear ridge that cross-
191 cuts the southern edge of Mt. Dent (Figure 3B). While this ridge has been proposed to be an AVR that has
192 propagated in to the southern flank of Mt. Dent by Cheadle et al.,(2012), its steep flanks, sharp curvilinear
193 spine with high acoustic backscatter, and lack of hummocky morphology (Figure 3B, C) are evidence of a
194 tectonic origin such as a fault-bound horst. Where this horst intersects the southern flank of Mt. Dent, it
195 continues up-slope as a deep V-shaped gully dissecting the massif (Figures 3A, B).

196 The southern end of the MCSC is similar to the northern segment, with bathymetry showing elevated
197 hummocky terrain characterized by bright acoustic backscatter, indicative of sediment-free volcanic terrain
198 along much of the axial floor (Figure 4A, B, C). We interpret the lack of sedimentation to be an indicator of
199 relatively young eruptive units compared with lower reflective seafloor that indicates thicker sediment
200 cover. Side-scan sonar imagery (Figure 4C) also reveals a brightly reflective but smooth area, surrounding
201 the elevated hummocky terrain. The highly reflective area continues southwards as a sinuous (in map view)
202 ribbon. This bright and sinuous feature follows the deepest part of the axial floor of the MCSC southwards
203 for over 5 km where it surrounds elevated areas of less reflective (i.e. more sediment covered) seafloor
204 (Figure 4C). The smooth morphology of this feature suggests it is a sheet flow with a long and thin runout.
205 In contrast with the adjacent darker seafloor, the bright acoustic backscatter indicates that it is virtually
206 sediment free and thus a relatively recent eruption. This assumption is confirmed by ground-truthing using
207 visual observations from the ROV (see Figure 4C for vehicle track in orange) that reveal the bright ribbon to
208 have a smooth lava surface with sparse sediment cover, whereas the darker and more elevated areas are flat-
209 topped 'islands' of seafloor, with thicker (~1 m) sediment cover, which are surrounded by the (relatively)
210 younger sheet-flow lava. The AUV-derived micro-bathymetry also shows this sheet flow to be cut by a
211 ~250 m high vertical fault scarp that downthrows the axial floor to the south (3D projection facing the
212 northwest in Figure 4B, NE-SW black line in Figure 4D). Close inspection of the side-scan sonar imagery
213 (Figure 4C) reveals an area of bright and diffuse backscatter at the base of the scarp and a continuation of
214 the lava flow, albeit with lower reflectivity, towards the southeast away from the bottom of the scarp and
215 down-slope into the nodal-deep basin. Visual observation by the ROV of fresh lava draping the top edge and
216 bottom of this scarp is evidence that it once formed a 'lavafall' over which the sheet lava flow once

217 cascaded as it flowed south into the nodal basin at the intersection with the Swan Island Fracture Zone. The
218 AUV bathymetry shows the scarp strikes across the axial valley in a SW-NE orientation as a fault and, from
219 the geometry of its trace as it intersects the topography, has a dip of 62° to the southeast. As such, it marks
220 the intersection between the southern end of the axis of the MCSC and the Swan Island Fracture Zone
221 (Figure 4D).

222 **4.2. Geology of the Mt. Dent OCC**

223 **4.2.1. Overview**

224 In contrast with the northern and southern segments of the MCSC, the central segment is dominated
225 by the ~16 km long (E-W), ~14.5 km wide Mt. Dent massif, that rises up to 2000 m above the adjacent
226 ~4800 m deep axial floor of the MCSC (Figure 5A). Its smooth surface is cut by N-S striking faults forming
227 scarps and incisions that strike across the massif (Figure 5A). In E-W profile, the domed and smooth
228 surface of Mt. Dent decreases in its maximum curvature from 8° km^{-1} at the base of its eastern flank, where
229 it dips 23° to the East, to $0.2^\circ \text{ km}^{-1}$ at its summit, where it is nearly horizontal (Figure 5A).

230 The geology of Mt. Dent has been determined from early dredging efforts, Alvin dives, and more
231 recent ROV investigations (*Stroup & Fox, 1981; Hayman et al., 2011*). Lithologies recovered from the
232 domed surface of Mt. Dent include serpentinitized harzburgite and dunite, deformed gabbro (including
233 mylonitized and amphibolite-facies meta-gabbros), fresh dolerite dikes and lavas. The western limit of the
234 massif is marked by a 25 km-long, N-S trending ridge with a series of parallel scarps along its crest and
235 orthogonal rills incising its eastern slope (Figure 5A). The smooth, lower southern flank of the massif has a
236 series of E-W striking, sub-parallel corrugations (Figure 5A, B). Immediately to the east of Mt. Dent, the
237 axial floor of the MCSC is characterized by hummocky terrain and circular volcanic edifices. The most
238 prominent of these is a ~2 km-diameter volcanic seamount, located 1.5 km east of the base of Mt. Dent
239 (Figure 5A). The junction between the hummocky volcanic terrain and smooth lower eastern flank of Mt.
240 Dent is marked by a curvilinear fault scarp that trends north-south and bends around the base of the massif
241 (Figure 5A, B).

242 We recognize the curvilinear scarp separating the smooth lower eastern flank of Mt. Dent from the
243 hummocky seafloor to the east as marking the location of the eastward dipping detachment fault that
244 exhumes deep-crustal and upper-mantle lithologies and displaces the neovolcanic hanging wall toward the
245 MCSC axial floor. Tucholke et al. (1998) refer to similar features on the MAR as the *termination*. However,
246 since the geological structures that we map here have a finite width, we adopt the term *termination zone* for

247 convenience. In turn, we define the N-S elongated ridge, forming the western limit of the Mt. Dent massif,
248 as the site of initiation of detachment faulting. Again, following the terminology coined by Tucholke et al.
249 (1998) to describe oceanic detachment faults, we refer to this structure as the *breakaway*. Note that the term
250 *breakaway* generally refers to any region where a fault initially breaks the Earth's surface, and has been
251 widely used to describe continental core complexes (e.g. *Davis*, 1980). Similarly, *termination* describes the
252 down-dip limit of a fault, and has been widely used in marine geology studies to describe where a
253 detachment fault emerges from the subsurface. The terms *hanging-wall cutoff* and *footwall cutoff* have also
254 been invoked for termination and breakaway zones in continental and oceanic core complexes
255 (*Allmendinger et al.*, 1981; *Escartin et al.*, 2017), but we do not adopt that terminology here.

256 **4.2.2 The Termination Zone**

257 We interpret the history of the termination zone from high-resolution bathymetry, slope mapping,
258 and acoustic backscatter imagery from the AUV of the base of the smooth, eastward-sloping flank of Mt.
259 Dent and the hummocky volcanic seafloor of the MCSC axis immediately to the east. In general the area has
260 low acoustic backscatter intensities except for a N-S trending, curvilinear “ribbon” and chaotic area of high
261 acoustic backscatter (Figure 6A, B). The bathymetry and slope-azimuth map (Figure 6A, C) show the
262 bright, curvilinear feature to be associated with a low, west-facing scarp that is ~10 m high at a depth of
263 approximately 4100 m. High acoustic backscatter is indicative of exposure of hard rock and rough seafloor,
264 whereas lower backscatter reflects sediment cover. High intensity acoustic backscatter is found to reduce
265 westwards, over a distance of ~100 m, to become similar to the low value of backscatter we find in the
266 surrounding sediment covered basement (Figure 6B). We interpret this change in backscatter to reflect
267 increasing acoustic attenuation by a wedge of sediment cover that thickens in the up-dip direction across the
268 termination zone. This reflects a history of detachment slip in which the accumulation of pelagic sediment
269 progressively attenuates the acoustic backscatter albedo of the detachment surface as it ages from initial
270 exposure immediately adjacent to the hanging wall. We note for context that a virtually identical feature has
271 been imaged (*MacLeod et al.*, 2009) and sampled (*Escartin et al.*, 2017) at the 13°20'N OCC (MAR).

272 The acoustic backscatter image and slope-azimuth map (Figure 6B, C) shows how the westward
273 dipping curvilinear active termination zone merges north of 18°22'N with a broader and more chaotic
274 terrain. The more chaotic terrain comprises patches of low-backscatter seafloor (i.e. sediment covered),
275 surrounded by a highly reflective (i.e. hard substrate) rugged and blocky seafloor,. When superimposed on
276 the micro-bathymetry, the acoustic backscatter image reveals these dark and angular patches to lie within
277 areas of highly reflective and steeply sloping seafloor, characteristic of recent slumping and displacement of
278 ‘rafts’ of sediment covered footwall to the east (Figure 7). The micro-bathymetry and slope-azimuth maps

279 (Figure 6A, C) also reveal another ~10 m high, N-S striking, westward-facing curvilinear fault scarp that
280 merges with the active termination zone to the south (black line in Figure 6D). The low acoustic backscatter
281 of this scarp shows it to be draped by a continuous sediment blanket and hence we infer that it is unlikely to
282 have been recently active.

283 4.2.3. Corrugations

284 Ship-board multibeam bathymetry data of the flanks of Mt. Dent reveal a series of parallel
285 corrugations, undulating grooves observable at the map scale (Figure 5A, B;) referred to as *mullion*
286 *structures* in some areas (e.g. *John*, 1987). The spatial orientations, described here, were determined via
287 analyses of the bathymetric data. These corrugations trend between 083° and 100° (Figure 5C),
288 approximately parallel to the spreading direction of the MCSC. Smaller-scale corrugations, observed from
289 the AUV-derived micro-bathymetry from near the base of the eastern side of Mt. Dent just west of the
290 termination zone, have a slightly different orientation of between 075° and 100°. The variation in
291 corrugation trend at Mt. Dent could be due to rheological responses during their evolution as the OCC was
292 exhumed (cf. *Escartin et al.*, 2017). Alternatively, the variation could be due to progressive changes in slip
293 direction and/or the result of deformation of the detachment fault surface after the corrugations formed, such
294 as by folding and/or flexure of the Mt. Dent massif. The data also reveal that these corrugations have a
295 wavelength of 100-200 m, an amplitude of 25-35 m, and lengths of up to 1.2 km (Figure 8).

296 The AUV bathymetry data also reveal arcuate structures superposed on the crests of the
297 corrugations, especially near the termination zone (Figure 8). These arcuate structures are ~10 m high, up to
298 1.5 km long, ~150 m apart, and concave downward toward the east. The origin of these is enigmatic, but we
299 note that they occur to the west of an arcuate bend in the trace of the termination zone (Figure 8), and may
300 result from debris deposited on the footwall by erosion of the hanging wall. We note that similar features are
301 described and sampled from the MAR 13°20'N OCC, by *Escartin et al.*, (2017) and propose that these are
302 common features of oceanic detachment faults where the hanging wall is eroded onto the emerging footwall.

303 The micro-bathymetry also reveals similarly oriented corrugations, albeit of a slightly more subdued
304 amplitude, located to the east of the termination zone (Figure 8). These features, termed here *ghost*
305 *corrugations* are continuous along strike with the corrugations to the west of the termination zone. Their
306 occurrence is enigmatic as they are formed in the rougher terrain of the thin trailing-edge of the hanging-
307 wall. As such, they are not ornamentations on the detachment surface, but might reflect the draping of the
308 thin trailing-edge of the hanging wall over topography of the yet-to-be exhumed footwall (see also *MacLeod*
309 *et al.*, 2009).

310 4.2.4. The upper slopes of Mt. Dent

311 The topography of the upper slopes of Mt. Dent, above a depth of 3000 m, contrast with the smooth
312 eastern and southern flanks of the massif by comprising a blocky and chaotic seafloor with east-facing steps
313 and gullies tens of metres deep (Figures 5B and 9). Similar chaotic terrain is reported from the upper slopes
314 of the 13°20' N OCC, MAR, by *Bonnemains et al.* (2017) and *Escartin et al.* (2017). Prominent lineaments
315 and scarps in this area are found by ROV observations and sampling to expose gabbro and serpentinized
316 ultramafic rocks (*Hodkinson et al.*, 2015), and are consistent with faulting of the basement. The most
317 prominent feature in this region is a series of conical mounds, up to 70 m tall and ~100 m metres in diameter
318 (Figure 9). These mounds form both the active and inactive vents in the Von Damm Vent Field (VDVF),
319 located at 81°47' W; 16°22.50' N (*Connelly et al.*, 2012; *Hodkinson et al.*, 2015). Primary vent fluid,
320 emitted from mounds of hydrothermal talc at 215°C, has a composition that indicates high-temperature
321 reaction between seawater, gabbro, and serpentinizing ultramafic rocks (*Hodkinson et al.*, 2015). The
322 VDVF dissipates up to 500 MW of thermal energy, cooling the interior of Mt. Dent (*Hodkinson et al.*,
323 2015).

324 The rocks surrounding the VDVF are mainly gabbroic with some serpentinized ultramafic rocks and
325 relatively fresh diabase dikes, all of which were recovered by ROV as reported in *Hodkinson et al.* (2015),
326 and which are consistent with previous sampling studies (*Stroup and Fox*, 1981). Another prominent but
327 hydrothermally inactive talc mound is located ~500 m to the east of the active VDVF and is surrounded by
328 smaller mounds of a similar origin. These are estimated from the observed thickness of the sediment cover
329 as well as analyses of the vents themselves to have ceased hydrothermal construction at least 20,000 years
330 ago (*Hodkinson et al.*, 2015), suggesting an extended history of hydrothermal activity at the VDVF.

331 The active hydrothermal mounds of the VDVF are aligned N-S and associated with several sets of
332 steep, NNW-SSE trending slopes, interpreted from the AUV-derived bathymetry, ROV observations, and
333 sampling of gabbroic outcrop as normal fault scarps (Figure 9). In addition, the micro-bathymetry maps
334 show cusp-shaped scarps and tongues of disturbed and hummocky material that are elongated down-slope
335 towards the east (Figure 9C). This has especially affected the active VDVF mounds, with the eastern slopes
336 showing signs of collapse and mass wasting. To the north of the VDVF, another tongue of blocks and
337 boulders extends to the east and widens into an E-W trending depression.

338

339

340 **4.2.5. The summit of Mt. Dent and Breakaway Zone**

341 At approximately 81°50'30" W, a N-S trending (structural) ridge marks the breakaway zone of Mt.
342 Dent (Figure 10A). Here, the summit area is characterized by a smooth region of depressions bound
343 between approximately N-S and E-W striking ridges and scarps (Figure 10B). These linear features, which
344 have been identified from the high-resolution multibeam bathymetry data, are likely to be the result of
345 sediment draping over underlying fault scarps.

346 To the west of the summit ridge, the scarps mainly dip towards the west in a series of steep steps that
347 form the western flank of the breakaway ridge. To the east of the breakaway ridge, the structures dip east
348 and form N-S elongated basins with smooth seafloor. Despite having only mapped a small area in high-
349 resolution by AUV, the shipboard multibeam bathymetry map shows the N-S trending structures continue
350 across the summit of Mt. Dent and along the breakaway zone (Figure 10A).

351 In this area, the AUV-derived micro-bathymetry also reveals clusters of pockmarks grouped in an E-
352 W trending band along the upper-southern flank of the summit region (blue dots on Figure 10B and inset
353 detail). The pockmarks are up to 10 m in diameter (Figure 10C). Observations by the ROV of the seafloor in
354 the vicinity of these larger pockmarks (yellow 'X' on Figure 10B) reveal steep-walled circular holes up to
355 75 cm in diameter and >1 m deep (Figure 10D). The presence of relatively undisturbed seafloor surrounding
356 the holes is indicative of material having been removed from the sub-seafloor. These features are
357 characteristic of fluid flow or degassing from the basement as seen in other seafloor environments, albeit in
358 those examples pockmarks are developed in thick sediments (*Hovland et al., 2002*).

359 **5. Discussion**

360 **5.1. Mt. Dent & OCC Evolution**

361 Mt. Dent shares structural similarities with many other OCCs, including a gabbro-dominated crustal
362 architecture and asymmetric domed surface that dips towards the rift axis where it terminates against
363 hummocky volcanic terrain (Figure 11). Like many of these OCCs, which also host hydrothermal systems,
364 the domed surface of Mt. Dent is characterized by corrugations spanning a range of scales from hundreds to
365 kilometers long and tens to hundreds of meters wide and with a narrow range of orientations. Most regional
366 analyses of OCC corrugations find that they trend roughly parallel to the spreading direction (e.g. *Smith and*
367 *Cann, 2006*). *Escartin et al. (2017)* and *Parnell-Turner et al. (2018)*, based on their work on the the 13°20'N
368 and 13°30'N MAR OCCs, suggested that the corrugations are the product of an integrated evolution of the

369 fault plane as it passes through the brittle-ductile transition. More generally, corrugated structures on any
370 fault surface can be due to the slip behaviour of faults in the brittle crust (*Resor and Meer, 2009*).

371 The MAR OCCs in particular exhibit detachment faults that, in places (especially 13°30' N), are cut
372 by high-angle faults and dike intrusions (*MacLeod et al., 2009*). MacLeod et al. (2009) proposed that these
373 dike intrusions “kill” detachment faults after they migrate into the axial valley, thereby allowing magmatism
374 from the adjacent AVRs to propagate across the OCC footwalls. Such a model may well apply to Mt. Dent
375 which shows evidence of tectonic instability in the: (i) disintegration of its termination zone, (ii) brittle
376 faulting across its upper flanks, summit, and breakaway, (iii) rifting of the southern flank, (iv) the
377 intersection of an axial volcanic ridge with its northern flank, and (v) likely magmatic intrusion deep within
378 the interior of Mt. Dent. We suggest that these features are indicative of Mt. Dent being in a terminal stage
379 of tectonic seafloor spreading, with slip on the detachment fault virtually ceased, and magmatic spreading
380 reasserting itself as the dominant mechanism of seafloor spreading.

381 **5.2. Cessation of Detachment Faulting**

382 Evidence for reduced tectonic activity of the detachment fault comes from near the most recently
383 exposed area of the termination zone where a thin band of acoustic reflectivity rapidly diminishes
384 westwards over a distance of ~100 m. We interpret this as a narrow (50-100 m) zone in which a hard and
385 rough basement exposed by slip on the detachment fault gives way to soft sediment cover. Our
386 interpretation is based on the reasoning that at a frequency of 200 kHz pelagic sediment attenuates the
387 backscattered signal from the EM2000 multibeam sonar by ~20-50 dB per metre, approximately equal to the
388 difference in acoustic backscatter between hard rock and soft sediment (*Stoll, 1985; Mitchell, 1993*). A
389 similar observation has been reported for the 13°20'N MAR OCC (e.g. *Parnell-Turner et al., 2018*), where
390 a reduction in backscatter-intensity across the termination zone is suggested to reflect the changing
391 thickness of sediment covering the fault surface as a result of slip of the detachment fault. There, the surface
392 of the emerging footwall is now covered by basaltic rubble eroded from the hanging wall (*Bonnemains et*
393 *al., 2017*).

394 Although the sedimentation rate for the central MCSC is unknown and is likely to be variable (e.g.
395 *Erikson et al., 1972*), the regional pelagic accumulation rate has been measured as <5 mm/ka (*Land, 1979*).
396 We estimate that, given these low sedimentation rates, a reasonable slip rate to cause the observed reduction
397 in acoustic backscatter intensity across the width of the active termination zone would be <5 mm/yr. Though
398 just an estimate we suggest that the pattern of sedimentation on the detachment surface indicates that the
399 slip rate is now very slow, if not inactive. In our interpretation, the few mm per year deficit between the

400 spreading rate and slip rate is increasingly accommodated by high-angle faulting and magmatism at this
401 location.

402 Further evidence that the detachment is currently inactive, or becoming inactive, is seen in the
403 termination zone to the north of 18°22'5"N. Here, the ribbon of bright acoustic backscatter indicates that the
404 active termination zone widens and becomes chaotic. We attribute this backscatter pattern to result from the
405 upper crustal dismemberment a weak footwall and brittle disintegration of the termination zone. Elsewhere,
406 the west-facing curvilinear fault scarp located 1-1.5 km west of the active termination zone (Figure 6) is
407 evidence of vertical dislocation; Stroup and Fox (1981) reported similar fault scarps from their observations
408 from the human occupied vehicle Alvin. An alternative interpretation of this particular fault splay is that it is
409 an antithetic normal fault or detachment fault splay formed after the footwall was denuded. In either case,
410 we interpret the bifurcation of faults in the termination zone as evidence of a transfer of stress following
411 strengthening (locking) of the detachment fault due either to its rheologic evolution, rotation to an
412 unfavorable orientation for slip, or both. As the hanging wall and footwall become more tightly coupled,
413 strain is transferred from the low-angle detachment fault to new and steeper dipping normal faults that cut
414 across the footwall, and the detachment fault surface disintegrates.

415 The central basin, forming the northern end of the southern segment of the MCSC, is dissected by a
416 NW-SE trending horst that rifts the southern flank of Mt. Dent. Such horsts are components of horst-and-
417 graben structures and rift shoulders that are predicted in models of extensional brittle failure of thick
418 lithosphere (e.g., *Lavier & Buck, 2002*). Similar features have been observed along the axis of the ultraslow
419 spreading Southwest Indian Ridge (*Sauter et al., 2013*). The intersection between the faults generating the
420 horst and the detachment fault could be a response to a non-transform offset proposed to bound the southern
421 end of Mt. Dent (*Macdonald and Holcombe, 1978*). The horst could also be a result of the generally melt-
422 poor environment (see below), thereby accommodating tectonic extension and potentially exposing as-yet
423 unidentified deeper crustal or upper mantle materials. Alternatively, in some respects the horst bears some
424 resemblance to the area near the Rainbow vent field (MAR 36°14'N) where detachment faulting and
425 magmatic sill emplacement have been identified in a non-transform offset (*Paulatto et al., 2015; Eason et*
426 *al., 2016*). Regardless, the fact that the horst is associated with normal faulting along the southern flank of
427 Mt. Dent is further evidence that the locus of extension is being transferred away from the detachment fault.

428 **5.3. Magmatism and OCC death**

429 Seismic imaging (*Van Avendonk et al., 2017*), seafloor observations (*Hayman et al., 2011*), and the
430 new data we present here show that the northern and southern segments of the central MCSC are currently

431 dominated by robust volcanic activity. The northern segment, which our data reveal is typified by a young,
432 hummocky AVR, circular volcanoes, and hydrothermal activity at the Beebe Vent Field, lies directly above
433 a low-velocity seismic anomaly of probable magmatic origin (*Van Avendonk et al., 2017*). The prominent
434 AVR in this location intersects the northern flank of Mt. Dent. Indeed, the presence of a wide field of fresh
435 hummocky volcanics along the northern AVR at its intersection with Mt. Dent is evidence for a robust
436 magma supply immediately adjacent to the OCC if not beneath it. Such magmatism would explain the
437 hydrothermal activity at the Von Damm Vent Field near the summit of Mt. Dent. Fluid flow is likely
438 facilitated by fracturing and opening of fluid-flow pathways over the possible magmatic intrusion and the
439 subsequent mining of heat from deep within the OCC (*Hodgkinson et al., 2015; McDermott et al., 2015*).
440 The fracturing and magmatism likely contributes further to a low P-wave seismic anomaly in the deep
441 subsurface below Mt. Dent (*Harding et al., 2017*).

442 Our data also show the area between the two volcanic segments of the MCSC, in the hanging wall of
443 the detachment fault, comprises hummocky volcanics including a circular seamount. Seismic studies show
444 this to be underlain by thin crust (*Van Avendonk et al., 2017; Harding et al., 2017*). We note that we cannot
445 rule out that these volcanic features have been tectonically juxtaposed against the footwall of Mt. Dent OCC
446 by the detachment fault. However, if these volcanic features indeed cross-cut the detachment fault then they
447 are further evidence that the OCC is being intruded by magma, contributing to the cessation of detachment
448 faulting.

449

450 **5.4. Hydrothermal Activity & the Mechanical Evolution of OCC interiors**

451 Following intrusion, *Hodgkinson et al. (2015)* estimated that the interior of Mt. Dent cools by 500°C
452 over 3800 and 6400 years. This estimate is based on a 10x10x3 km volume and a rate of about 0.3 m³s⁻¹
453 assuming the dominant lithology is gabbro (*Arafin and Singh, 2016*) and that chemically produced heat from
454 serpentinization is not significant. Such rapid cooling will deepen the brittle-ductile transition within the
455 OCC footwall, enhancing further brittle deformation, fluid flow, and weakening of the interior of the massif.

456 Faulting, fracturing and fluid flow are a response to magmatic intrusion within the OCC and also a
457 reflection of the changing stress field as the OCC is flexurally exhumed and spreads off axis. However, the
458 brittle deformation and fluid flow are also likely to change the effective stress within the Mt. Dent massif,
459 thereby further weakening the interior of the OCC relative to the detachment fault to the east. Such a strain
460 evolution has also been proposed for the Atlantis Massif, where exhumation is accompanied by flexural
461 uplift and rotation of normal faults into a mechanically favorable high-angle orientation, accompanied by
462 internal strain within the OCC (*Karson et al., 2006*). Also at the Atlantis Massif, fluids flow through

463 fractures and faults within the OCC feeding the Lost City Field vents (*Denny et al.*, 2016), and may also
464 cause a change in effective stress due to the overall low-permeability environment (*Hirose and Hayman*,
465 2008). The presence of pockmarks distributed across the southern flank of Mt. Dent potentially indicates an
466 even broader fluid-flow regime associated with internal deformation of the OCC. We note that the
467 pockmarks themselves do not align along individually mapped faults, illustrating that the permeability and
468 fluid flow regime is more widespread within the faulted regions, perhaps in the distributed fractures of
469 damage zones surrounding the faults themselves.

470 The idea that the detachment is becoming inactive is also consistent with modelling that indicates
471 that, as conditions become less favorable for continued OCC growth (e.g. through diking and magmatic
472 intrusion across the detachment fault and into the hanging wall), new high-angle faults begin to dissect the
473 OCC (*Behn and Ito*, 2008). As discussed above, such a transition may have already occurred at Mt. Dent, as
474 suggested by the occurrence of predominately N-S striking normal faults and recent slumping higher up on
475 the domed massif, the hydrothermal venting, and the clusters of pockmarks indicating fluid released from
476 within the upper massif by brittle faulting. We note similar tectonic features, other than perhaps the
477 pockmarks, have been reported from OCCs elsewhere, including the FUJI Dome, an inactive OCC on the
478 Southwest Indian Ridge (*Searle et al.*, 2003), and the Rainbow massif on the northern MAR (*Paulatto et al.*,
479 2015), and suggest this style of faulting is associated with OCC termination.

480 **5.5. OCC Evolution at Ultraslow Spreading Centers**

481 Before explaining how our interpretations and hypotheses are consistent with current views of
482 ultraslow spreading centers, we note that there are alternative hypotheses for the origin of several of the key
483 geologic features. Though singularly we cannot rule these hypotheses out, we find them to be less consistent
484 both with our data and with the model framework we describe below. For example, the detachment could be
485 currently slipping at an unchanged rate, but then we would expect more irregular, unsedimented areas of the
486 detachment surface near the termination zone as seen, for example, at the Kane transform OCC of the MAR
487 (*Tucholke et al.*, 2013). Furthermore, if the detachment was still active, we would expect sedimentary wedge
488 and hanging-wall normal fault relations more consistent with a Coulomb Wedge model (*Hayman et al.*,
489 2003; *Olive et al.*, 2019); we observe neither of these features. Magmatic diking could have formed the
490 southern horst, but we observe no neovolcanic zone associated with this feature on its trace along the
491 seafloor. Lastly, lithospheric heat (*Lowell*, 2018) and/or heat from serpentinization (*Fruh-Green et al.*,
492 2003) could be driving the hydrothermal system. However, the fluid and mineral chemistry at the VDVF
493 (*Hodgkinson et al.*, 2015; *Webber et al.*, 2015; *McDermott et al.*, 2015), the spatial coincidence with the
494 nearby AVR, the similarities of the setting with the magmatic sills seismically imaged below the possibly

495 analogous Rainbow vent field on the MAR (*Canales et al.*, 2017), and arguments that venting requires
496 magmatic heat (*Allen and Seyfried*, 2004), all lead us to suspect there are gabbroic intrusions from the
497 mantle intruding the OCCs.

498 We now describe how our interpretations and hypotheses are oddly consistent with current views of
499 ultraslow seafloor spreading. Ultraslow spreading centers worldwide are thought to have relatively thin
500 crusts and great axial depths, a reflection of generally low melt production from a mantle with a low
501 potential temperature (e.g., *Klein & Langmuir*, 1987; *Dick et al.*, 2003). The MCSC falls within this class of
502 ultraslow spreading centers, and seafloor older than 10 Ma is dominated by exhumed mantle (*Grevenmeyer et*
503 *al.*, 2018), and serpentinitized peridotites from the axial deep resemble those from the Southwest Indian and
504 Gakkel Ridges (*Mallick et al.*, 2014). Yet, Mt. Dent is also similar to OCCs on other ultraslow spreading
505 ridges, such as Atlantis Bank on the Southwest Indian Ridge (SWIR) which despite the overall melt-poor
506 environment have drill cores dominated by plutonic gabbro bodies intruded into an ultramafic host rock
507 (*Dick et al.*, 2000).

508 With an E-W length of 14 km from the termination zone to the breakaway, and a full spreading rate
509 of 15 mm/yr, we calculate that the Mt. Dent OCC was active for between about 1 and 2 myr, given that the
510 youngest edge of magnetic anomaly 2 (~1.64 Ma, *Leroy et al.*, 2000) coincides approximately with the
511 breakaway region (*Hayman et al.*, 2011). We note that even though magnetic anomalies are highly
512 asymmetric in their character from west to east across Mt. Dent, Anomalies 2-3 are roughly symmetrically
513 located on the conjugate sides of the spreading center (*Rosencrantz*, 1988; *LeRoy et al.*, 2000; *Hayman et*
514 *al.*, 2011). Given that the eastern flank of the central MCSC is dominated by volcanic rocks and the western
515 side by detachment faulting at Mt. Dent, the symmetry in spreading indicates that tectonic extension on the
516 OCC detachment fault accommodates ~50% of the plate separation while magmatic accretion
517 accommodates the other 50%.

518 In the terminology of *Buck et al.* (2005) the MCSC seafloor spreading is thus described by an M (ratio of
519 tectonic to magmatic spreading) of 0.5. *Olive et al.* (2010) argue that termination of OCC growth is favored
520 where this proportion of magmatism is intruded into the brittle lithosphere deep within the footwall of an
521 OCC. Thus, ironically, even though overall the MCSC is a melt-poor environment, local magmatism can
522 accommodate enough seafloor spreading so as to disfavor OCC development as is observed at faster
523 spreading centers worldwide.

524

525 5. Conclusions

526 Interpretations of multibeam bathymetric and side-scan sonar data highlight how a range of tectonic
527 and magmatic processes are impacting a prominent OCC, Mt. Dent, that defines the central east flank of the
528 ultraslow-spreading MCSC. Extensive and recent volcanism in the northern axial valley of the MCSC leads
529 to southward prolongation of an axial volcanic ridge (AVR) into the northern flank of the OCC. In the
530 southern axial valley an extensional fault system generates a horst that continues northwards into the
531 southern flank of the massif. Faulting and distributed fracturing cut across the OCC-bounding detachment
532 surface leading to significant mass wasting in several locations. Pelagic sedimentation unevenly drapes the
533 corrugated detachment surface, but in a manner that suggests recent detachment exhumation at a slower rate
534 than tectonic spreading. The propagation of magmatism and faulting into the into the massif's flanks from
535 the north and south allows the transfer of strain from the OCC detachment fault to the steeply dipping
536 normal faults that dissect the flexed massif. Deep-rooted hydrothermal activity cools the interior of OCCs
537 and deepens the ductile/brittle transition, increasing the volume of footwall that undergoes brittle
538 extensional deformation and further weakening the footwall. Some alternative hypotheses cannot be ruled
539 out, including possible ongoing detachment faulting, significant contributions from other heat sources to the
540 hydrothermal system, and magmatic intrusions associated with the southern horst. However, our favored
541 interpretations are in broad agreement with both existing subsurface geophysical data and geodynamic
542 models for OCC evolution, whereas collectively the alternatives are not. Namely, that models predict that
543 OCC termination occurs when magmatic intrusion and diking into the brittle part of an OCC footwall
544 exceeds 50%. This model prediction, when applied to the MCSC, leads to the conclusion that despite the
545 melt-starved nature of ultraslow spreading ridges, tectonic spreading by OCC growth is terminated by an
546 increase in magmatic activity, as is observed for faster spreading centers.

547 Acknowledgments

548 We are grateful to the captain, officers and crew of the *RRS James Cook*, and to the operators of the
549 ROV Isis and Autosub6000 during cruises JC044 and JC081. This study was funded by the Natural
550 Environment Research Council (NERC), UK, Grant NE/101442X/1 (Murton). Searle's participation was
551 funded in part by a Leverhulme Emeritus Fellowship and in part by a Royal Society travel grant. Hayman
552 was supported by (US National Science Foundation) OCE-0961775 and OCE-1356895 and assisted with the
553 final preparation of this manuscript while a Program Director at the National Science Foundation. We are
554 grateful to Michele Paulatto, John Jamieson, Rob Sohn and an anonymous associate editor for their very
555 helpful reviews. All data from cruise JC44 and JC81 are archived at the NERC's British Oceanographic

556 Data Center (www.bodc.ac.uk). Geographically registered grids of the bathymetry and sidescan sonar
557 images are available from the supplementary data.

558 **References**

559 Allen, D.E. & Seyfried Jr., W.E. (2004). Serpentinization and heat generation: constraints from Lost City
560 and Rainbow hydrothermal systems1. *Geochimica et Cosmochimica Acta*, 68, 1347-1354.

561 Allmendinger, R.W., Sharp, J.W., Von Tish, D., Serpa, L., Brown, L., Kaufman, S., Oliver, J., Smith, R.B.
562 (1981). Cenozoic and Mesozoic structure of the eastern Basin and Range province, Utah, from COCORP
563 seismic-reflection data. *Geology*, 11, 532-536.

564 Arafin, S. & Singh., R. N. (2016). Thermal and Transport Properties of Mafic and Ultramafic Rocks of
565 Oman Ophiolite. *SQU Journal for Science*, 21, 69-81

566 Behn, M. D., & Ito, G. (2008). Magmatic and tectonic extension at mid-ocean ridges: 1. Controls on fault
567 characteristics. *Geochemistry, Geophysics, Geosystems*, 9(8), 1–22. <https://doi.org/10.1029/2008GC001965>

568 Blondel, P. & Murton, B. (1997). Handbook of Seafloor Sonar Imagery. *Wiley Praxis Series in Remote*
569 *Sensing*, London, pp. 314, ISBN: 9780471962175

570 Bonnemains, D., Escartin, J., Mével, C., Andreani, M. and Verlaquet, A., 2017. Pervasive silicification and
571 hanging wall overplating along the 13° 20' N oceanic detachment fault (Mid-Atlantic R
572 idge). *Geochemistry, Geophysics, Geosystems*, 18(6), pp.2028-2053.

573 Buck, W. R., Lavier, L. L., & Poliakov, A. N. B. (2005). Modes of faulting at mid-ocean ridges. *Nature*,
574 434(7034), 719–723. <https://doi.org/10.1038/nature03358>

575 Canales, J. P., Dunn, R. A., Arai, A. & Sohn, R. A. (2017). Seismic imaging of magma sills beneath an
576 ultramafic-hosted hydrothermal system. *Geology* 45(5): 451-454.

577 Cann, J.R. (1968). Geological processes at mid-ocean ridge crests. *Geophysical Journal*
578 *International*, 15(3), 331-341.

579 Cann, J. R., Blackman, D. K., Smith, D. K., McAllister, E., Janssen, B., Mello, S., et al. (1997). Corrugated
580 slip surfaces formed at ridge–transform intersections on the MAR. *Nature*. <https://doi.org/10.1038/385329a0>

581 Cannat, M. (1993). Emplacement of mantle rocks in the seafloor at mid-ocean ridges. *Journal of*

- 582 *Geophysical Research*, 98(B3), 4163–4172. <https://doi.org/10.1029/92JB02221>
- 583 Cannat, M., Sauter, D., Mendel, V., Ruellan, E., Okino, K., Escartin, J., et al. (2006). Modes of seafloor
584 generation at a melt-poor ultraslow-spreading ridge. *Geology*, 34(7), 605–608.
585 <https://doi.org/10.1130/G22486.1>
- 586 Cheadle, M. J., John, B. E., German, C. R., & Kuszniir, N. J. (2012). *The Death Throes of Ocean Core*
587 *Complexes: Examples from the Mid-Cayman Spreading Center*. Paper presented at the American
588 Geophysical Union Fall meeting, San Francisco.
- 589 Connelly, D. P., Copley, J. T., Murton, B. J., Stansfield, K., Tyler, P. a, German, C. R., et al. (2012).
590 Hydrothermal vent fields and chemosynthetic biota on the world’s deepest seafloor spreading center. *Nature*
591 *Communications*, 3, 620. <https://doi.org/10.1038/ncomms1636>
- 592 Davis, G. H. (1980). Structural characteristics of metamorphic core complexes, southern
593 Arizona. *Cordilleran metamorphic core complexes: Geological Society of America Memoir*, 153, 35-77.
- 594 deMartin, B. J., Sohn, R. A., Canales, J. P., & Humphris, S. E. (2007). Kinematics and geometry of active
595 detachment faulting beneath the Trans-Atlantic Geotraverse (TAG) hydrothermal field on the MAR.
596 *Geology*, 35(8), 711–714; [https://doi.org: 10.1130/G23718A.23711](https://doi.org/10.1130/G23718A.23711).
- 597 Denny, A.R., Kelley, D.S. and Früh-Green, G.L. (2016). Geologic evolution of the Lost City hydrothermal
598 field. *Geochemistry, Geophysics, Geosystems*, 17(2), pp.375-394.
- 599 Dick, H.J., Natland, J.H., Alt, J.C., Bach, W., Bideau, D., Gee, J.S., Haggas, S., Hertogen, J.G., Hirth, G.,
600 Holm, P.M. and Ildefonse, B. (2000). A long in situ section of the lower ocean crust: results of ODP Leg
601 176 drilling at the Southwest Indian Ridge. *Earth and planetary science letters*, 179(1), pp.31-51.
- 602 Dick, H.J., Lin, J. and Schouten, H. (2003). An ultraslow-spreading class of ocean ridge. *Nature*, 426(6965),
603 p.405.
- 604 Eason, D. E., Dunn, R. A., Pablo Canales, J., & Sohn, R. A. (2016). Segment-scale variations in seafloor
605 volcanic and tectonic processes from multibeam sonar imaging, Mid-Atlantic Ridge Rainbow region (35°
606 45′–36° 35′ N). *Geochemistry, Geophysics, Geosystems*, 17(9), 3560-3579.
- 607 Edgar, N. T., Dillon, W. P., Parson, L. M., Scanlon, K. M., C. L. Jacobs K. M., & Holcombe, T. L.
608 (1991). GLORIA sidescan sonar image and interpretation of the central Cayman trough, northwestern
609 Caribbean Sea, U.S. Geological Survey Miscellaneous Field Studies Map, MF-2083 A, 3 sheets.

- 610 Edmonds, H. N., Michael, P. J., Baker, E. T., Connelly, D. P., Snow, J. E., Langmuir, C. H., et al. (2003).
611 Discovery of abundant hydrothermal venting on the ultraslow- spreading Gakkel ridge in the Arctic. *Nature*
612 *421* (6920): 252-256.
- 613 Erickson, A. J., Hellsley, C. E., & Simmons, G. (1972). Heat Flow and Continuous Seismic Profiles in the
614 Cayman Trough and Yucatan Basin. *Geological Society of America Bulletin*, *83*, 1241-1260.
- 615 Escartin, J., Mevel, C., Petersen, S., Bonnemaïn, D., Cannat, M., Andreani, M., et al. (2017). Tectonic
616 structure, evolution, and the nature of oceanic core complexes and their detachment fault zones (13 degrees
617 20 ' N and 13 degrees 30 ' N, Mid Atlantic Ridge). *Geochemistry Geophysics Geosystems*, *18* (4), 1451-
618 1482. <https://doi.org/10.1002/2016gc006775>
- 619 Escartin, J., Smith, D. K., Cann, J., Schouten, H., Langmuir, C. H., & Escrig, S. (2008). Central role of
620 detachment faults in accretion of slow-spreading oceanic lithosphere. *Nature*, *455*, 790-795.
621 <https://doi.org/10.1038/nature07333>
- 622 Früh-Green, G. L., Kelley, D.S., Bernasconi, S.M., Karson, J.A., Ludwig, K.A., Butterfield, D.A., et al.
623 (2003). 30,000 years of hydrothermal activity at the Lost City vent field. *Science* *301*: 495-498.
- 624 Garcés, M. and Gee, J.S. (2007). Paleomagnetic evidence of large footwall rotations associated with low-
625 angle faults at the Mid-Atlantic Ridge. *Geology*, *35*(3), 279-282.
- 626 German, C. R., Bowen, A., Coleman, M. L., Honig, D. L., Huber, J. A., Jakuba, M. V., et al. (2010).
627 Diverse styles of submarine venting on the ultraslow spreading Mid-Cayman Rise. *Proceedings of the*
628 *National Academy of Sciences of the United States of America*, *107* (32), 14020-14025.
629 <https://doi.org/10.1073/pnas.1009205107>
- 630 Grevemeyer, I., Hayman, N. W., Peirce, C., Schwardt, M., Van Avendonk, H. J. A., Dannowski, A., &
631 Papenberg, C. (2018). Episodic magmatism and serpentinized mantle exhumation at an ultraslow-spreading
632 center. *Nature Geoscience*, *11* (6), 444. <https://doi.org/10.1038/s41561-018-0124-6>
- 633 Harding, J. L., Van Avendonk, H. J. A., Hayman, N. W., Grevemeyer, I., & Peirce, C. (2017). Magmatic-
634 tectonic conditions for hydrothermal venting on an ultraslow-spread oceanic core complex. *Geochemistry,*
635 *Geophysics, Geosystems* *45*: 3-6. <https://doi.org/10.1130/G39045.1>
- 636 Hayman, N.W., Knott, J.R., Cowan, D.S., Nemser, E. and Sarna-Wojcicki, A.M., 2003. Quaternary low-
637 angle slip on detachment faults in Death Valley, California. *Geology*, *31*(4), pp.343-346.

- 638 Hayman, N. W., Grindlay, N. R., Perfit, M. R., Mann, P., Leroy, S., & de Lépinay, B. M. (2011). Oceanic
639 core complex development at the ultraslow spreading Mid-Cayman Spreading Center. *Geochemistry,*
640 *Geophysics, Geosystems, 12*(3), n/a-n/a. <https://doi.org/10.1029/2010GC003240>
- 641 Hirose, T., & Hayman, N. W. (2008). Structure, permeability, and strength of a fault zone in the footwall of
642 an oceanic core complex, the Central Dome of the Atlantis Massif, MAR, 30°N. *Journal of Structural*
643 *Geology, 30*(8), 1060–1071. <https://doi.org/10.1016/j.jsg.2008.04.009>
- 644 Hodgkinson, M. R. S., Webber, A. P., Roberts, S., Mills, R. A., Connelly, D. P., & Murton, B. J. (2015).
645 Talc-dominated seafloor deposits reveal a new class of hydrothermal system. *Nature Communications, 6*,
646 [doi:10.1038/ncomms10150](https://doi.org/10.1038/ncomms10150)
- 647 Hovland, M., Gardner, J. & Judd, A. (2002). The significance of pockmarks to understanding fluid flow
648 processes and geohazards. *Geofluids, 2*(2), 127–136.
- 649 Ildefonse, B., Blackman, D. K., John, B. E., Ohara, Y., Miller, D. J., MacLeod, C. J., et al. (2007). Oceanic
650 core complexes and crustal accretion at slow-spreading ridges. *Geology, 35*(7), 623–626.
651 <https://doi.org/10.1130/G23531A.1>
- 652 John, B. E. (1987). Geometry and evolution of a mid-crustal extensional fault system: Chemehuevi
653 Mountains, southeastern California. *Geological Society, London, Special Publications, 28*(1), 313-335.
- 654 Karson, J. A., & Dick, H. J. B. (1983). Tectonics of ridge-transform intersections at the Kane fracture zone.
655 *Marine Geophysical Researches, 6*(1), 51–98. <https://doi.org/10.1007/BF00300398>
- 656 Karson, J.A., Früh-Green, G.L., Kelley, D.S., Williams, E.A., Yoerger, D.R. and Jakuba, M. (2006).
657 Detachment shear zone of the Atlantis Massif core complex, Mid-Atlantic Ridge, 30 N. *Geochemistry,*
658 *Geophysics, Geosystems, 7*(6).
- 659 Klein, E. M., and C. H. Langmuir (1987), Global correlations of ocean ridge basalt chemistry with axial
660 depth and crustal thickness, *Journal of Geophysical Research, 92*, 8089–8115.
- 661 Land, L. S. (1979). Fate of reef-derived sediment on the North Jamaican island slope. *Marine Geology,*
662 *29*(1-4), 55-71. [https://doi.org/10.1016/0025-3227\(79\)90102-6](https://doi.org/10.1016/0025-3227(79)90102-6)
- 663 Lavier, L. L., & Buck, R. (2002). Half graben versus large-offset low-angle normal fault: Importance of
664 keeping cool during normal faulting. *Journal of Geophysical Research, 107*(B6), ETG8 1-13,
665 <https://doi.org/10.1029/2001JB000513>.

- 666 Lavier, L. L., Buck, W. R., & Poliakov, a. (1999). Self-consistent rolling-hinge model for the evolution of
667 large-onset low-angle normal faults, *Geology*, 27(12), 1127–1130.
- 668 Leroy, S., Mauffret, A., Patriat, P., & Mercier De Lépinay, B. (2000). An alternative interpretation of the
669 Cayman trough evolution from a reidentification of magnetic anomalies. *Geophysical Journal International*,
670 141(3), 539–557. <https://doi.org/10.1046/j.1365-246X.2000.00059.x>
- 671 Lowell, R. P. (2017). A fault-driven circulation model for the Lost City Hydrothermal Field. *Geophysical*
672 *Research Letters*, 44(6), 2703-2709.
- 673 Macdonald, K.C. and Luyendyk, B.P. (1977). Deep-tow studies of the structure of the Mid-Atlantic Ridge
674 crest near latitude 37°N. *Geological Society of America Bulletin*, 88(5), 621-636.
- 675 Macdonald, K. C. & Holcombe, T. L. (1978). Inversion of magnetic-anomalies and sea-floor spreading in
676 the Cayman Trough. *Earth and Planetary Science Letters*, 40 (3): 407-414.
- 677 MacLeod, C. J., Searle, R. C., Murton, B. J., Casey, J. F., Mallows, C., Unsworth, S. C., Achenbach, K., &
678 Harris, M. (2009). Life cycle of oceanic core complexes. *Earth and Planetary Science Letters*, 287 (3–4),
679 333–344. <https://doi.org/10.1016/j.epsl.2009.08.016>
- 680 Mallick, S., Dick, H. J., Sachi-Kocher, A., & Salters, V. J. (2014). Isotope and trace element insights into
681 heterogeneity of subridge mantle. *Geochemistry, Geophysics, Geosystems*, 15(6), 2438-2453.
- 682 Mann, P., DeMets C., & Wiggins-Grandison, M (2007). Toward a better understanding of the Late Neogene
683 strike-slip restraining bend in Jamaica: geodetic, geological, and seismic constraints. *Tectonics of Strike-Slip*
684 *Restraining and Releasing Bends*. Cunningham, W. D. & Mann, P. 290: 239-253.
- 685 McDermott, J. M., Seewald, J. S., German, C. R., & Sylva, S. P. (2015). Pathways for abiotic organic
686 synthesis at submarine hydrothermal fields. *Proceedings of the National Academy of Sciences*, 112(25),
687 7668-7672.
- 688 McDermott, J. M., Sylva, S. P., Ono, S., German, C. R., & Seewald, J. S. (2018). Geochemistry of fluids
689 from Earth's deepest ridge-crest hot-springs: Piccard hydrothermal field, Mid-Cayman Rise. *Geochimica Et*
690 *Cosmochimica Acta*, 228, 95-118. <https://doi:10.1016/j.gca.2018.01.021>
- 691 Michael, P.J., Langmuir, C.H., Dick, H.J.B., Snow, J.E., Goldstein, S.L., Graham, D.W., Lehnert, K.,
692 Kurras, G., Jokat, W., Mühe, R. and Edmonds, H.N. (2003). Magmatic and amagmatic seafloor generation
693 at the ultraslow-spreading Gakkel ridge, Arctic Ocean. *Nature*, 423(6943), p.956.

- 694 Mitchell, N. C. (1993). A model for attenuation of backscatter due to sediment accumulations and its
695 application to determine sediment thickness with GLORIA sidescan sonar. *Journal of Geophysical*
696 *Research*, 98, 22,477 - 422,493.
- 697 Morris, A., Gee, J.S., Pressling, N., John, B.E., MacLeod, C.J., Grimes, C.B. and Searle, R.C. (2009).
698 Footwall rotation in an oceanic core complex quantified using reoriented Integrated Ocean Drilling Program
699 core samples. *Earth and Planetary Science Letters*, 287(1), 217-228.
- 700 Murton, B. J., Huhnerbach, V., & Garrard, J. (2012). Exploring ultradeep hydrothermal vents in the Cayman
701 Trough by ROV. *Sea Technology*, (SEPTEMBER 2012), 15–20. Retrieved from [http://www.sea-](http://www.sea-technology.com/features/2012/0912/hydrothermal_vents.php)
702 [technology.com/features/2012/0912/hydrothermal_vents.php](http://www.sea-technology.com/features/2012/0912/hydrothermal_vents.php)
- 703 Mutter, J.C. and Karson, J.A. (1992). Structural processes at slow-spreading ridges. *Science*, 257 (5070),
704 627 - 634
- 705 Olive, J.-A., Behn, M. D., & Tucholke, B. E. (2010). The structure of oceanic core complexes controlled by
706 the depth distribution of magma emplacement. *Nature Geoscience*, 3 (7), 491–495.
707 <https://doi.org/10.1038/ngeo888>
- 708 Olive, J. A., Parnell-Turner, R., Escartín, J., Smith, D. K., & Petersen, S. (2019). Controls on the seafloor
709 exposure of detachment fault surfaces. *Earth and Planetary Science Letters*, 506, 381-387.
- 710 Parnell-Turner, R., Escartin, J., Olive, J. A., Smith, D. K., & Petersen, S. (2018). Genesis of corrugated fault
711 surfaces by strain localization recorded at oceanic detachments. *Earth and Planetary Science Letters*, 498,
712 116-128. <https://doi.org/10.1016/j.epsl.2018.06.034>
- 713 ~~Parnell-Turner, R., Sohn, R. A., Peirce, C., Reston, T. J., MacLeod, C. J., Searle, R. C., & Simão, N. M.~~
714 ~~(2017). Oceanic detachment faults generate compression in extension. *Geology*.~~
715 ~~<https://doi.org/10.1130/G39232.1>~~
- 716 Paulatto, M., Canales, J.P., Dunn, R. A., & Sohn, R. A. (2015). Heterogeneous and asymmetric crustal
717 accretion: New constraints from multibeam bathymetry and potential field data from the Rainbow area of
718 the MAR (36°15'N). *Geochem. Geophys. Geosys.*, 16. <https://doi.org/10.1002/2015GC005743>
- 719 Resor, P.G. and Meer, V.E., 2009. Slip heterogeneity on a corrugated fault. *Earth and Planetary Science*
720 *Letters*, 288(3-4), pp.483-491.
- 721 Reston, T.J., Weinrebe, W., Grevemeyer, I., Flueh, E.R., Mitchell, N.C., Kirstein, L., Kopp, C. and Kopp,

- 722 H., 2002. A rifted inside corner massif on the Mid-Atlantic Ridge at 5 S. *Earth and Planetary Science*
723 *Letters*, 200(3-4), pp.255-269.
- 724 Rosencrantz, E., Ross, M. I., & Sclater, J. G. (1988). Age and spreading history of the Cayman Trough as
725 determined from depth, heat-flow, and magnetic-anomalies. *Journal of Geophysical Research-Solid Earth*
726 and Planets 93 (B3): 2141-2157.
- 727 Sauter, D., Carton, H., Mendel, V., Munsch, M., Rommevaux-Jestin, C., Schott, J.J. and Whitechurch, H.,
728 2004. Ridge segmentation and the magnetic structure of the Southwest Indian Ridge (at 50 30' E, 55 30' E
729 and 66 20' E): Implications for magmatic processes at ultraslow-spreading centers. *Geochemistry,*
730 *Geophysics, Geosystems*, 5(5).
- 731 Sauter, D., Cannat, M., Rouméjon, S., Andreani, M., Birot, D., Bronner, A., et al. (2013). 11 Myr-
732 continuous exhumation of mantle-derived rocks at the Southwest Indian Ridge. *Nature Geoscience*,
733 [https://doi.org/ 10.1038/NGEO1771](https://doi.org/10.1038/NGEO1771).
- 734 Schouten, H., Smith, D. K., Cann, J. R., & Escartín, J. (2010). Tectonic versus magmatic extension in the
735 presence of core complexes at slow-spreading ridges from a visualization of faulted seafloor topography.
736 *Geology*, 38(7), 615–618. <https://doi.org/10.1130/G30803.1>
- 737 Searle, R. C., Cannat, M., Fujioka, K., Mevel, C., Fujimoto, H., Bralee, A., & Parson, L. (2003). The FUJI
738 Dome: A large detachment fault near 64°E on the very slow-spreading southwest Indian Ridge.
739 *Geochemistry, Geophysics, Geosystems*, 4 (8), 9105. [https:// doi.org/10.1029/2003GC000519](https://doi.org/10.1029/2003GC000519).
- 740 Searle, R. C., Murton, B. J., Achenbach, K., LeBas, T., Tivey, M., Yeo, I., et al. (2010). Structure and
741 development of an Axial Volcanic Ridge: MAR, 45°N. *Earth and Planetary Science Letters*, 299, 228-241.
742 <https://doi.org/10.1016/j.epsl.2010.09.003>
- 743 Shaw, P. R., & Lin, J. (1993). Causes and consequences of variations in faulting style at the MAR. *Journal*
744 *of Geophysical Research*, 98 (B12), 21,839-821,851.
- 745 Smith, D. K., & Cann, J. R. (1990). Hundreds of small volcanoes on the median valley floor of the MAR at
746 24-30°N. *Nature*, 348, 152-155.
- 747 Smith, D. K., Cann, J. R., & Escartín, J. (2006). Widespread active detachment faulting and core complex
748 formation near 13 N on the Mid-Atlantic Ridge. *Nature*, 442(7101), 440.
- 749 Stoll, R. D. (1985). Marine sediment acoustics. *J. Acoust. Soc. Am*, 77, 1789-1799.

- 750 Stroup, J. B., & Fox, P. J. (1981). Geologic Investigations in the Cayman Trough: Evidence for Thin
751 Oceanic Crust along the Mid-Cayman Rise. *The Journal of Geology*, 89(4), 395–420.
- 752 Sykes, L.R. (1967). Mechanism of earthquakes and nature of faulting on the mid-oceanic ridges. *Journal of*
753 *Geophysical Research*, 72 (8), 2131-2153.
- 754 Tao, C., Lin, J., Guo, S., Chen, Y. J., Wu, G., Han, X., et al. (2012). First active hydrothermal vents on an
755 ultraslow-spreading center: Southwest Indian Ridge. *Geology* 40 (1): 47-50. [https://doi.org/](https://doi.org/10.1130/g32389.1)
756 [10.1130/g32389.1](https://doi.org/10.1130/g32389.1)
- 757 ten Brink, U., Coleman, D., & Dillon, W. P. (2002). The nature of the crust under Cayman Trough from
758 gravity. *Marine and Petroleum Geology*, 19, 971-987.
- 759 Tucholke, B. E., Lin, J., & Kleinrock, M. C. (1998). Megamullions and mullion structure defining oceanic
760 metamorphic core complexes on the MAR. *Journal of Geophysical Research*, 103(B5), 9857–9866.
761 <https://doi.org/10.1029/98JB00167>
- 762 Tucholke, B. E., & Lin, J. (1994). A geological model for the structure of ridge segments in slow spreading
763 ocean crust. *Journal of Geophysical Research*, 99(B6), 11937–11958. <https://doi.org/10.1029/94JB00338>
- 764 Tucholke, B. E., Behn, M. D., Buck, W. R., & Lin, J. (2008). Role of melt supply in oceanic detachment
765 faulting and formation of megamullions. *Geology*, 36(6), 455. <https://doi.org/10.1130/G24639A.1>
- 766 Tucholke, B. E., Humphris, S. E., & Dick, H. J. (2013). Cemented mounds and hydrothermal sediments on
767 the detachment surface at Kane Megamullion: A new manifestation of hydrothermal venting. *Geochemistry,*
768 *Geophysics, Geosystems*, 14(9), 3352-3378.
- 769 Van Avendonk, H. J. A., Hayman, N. W., Harding, J. L., Grevermeyer, I., Peirce, C., & Dannowski, A.
770 (2017). Seismic structure and segmentation of the axial valley of the Mid-Cayman Spreading Center.
771 *Geochemistry, Geophysics, Geosystems*, 18, 2149–2161. <https://doi.org/10.1002/2017GC006873>
- 772 Webber, A. P., S. Roberts, B. J. Murton, and M, R. S. Hodgkinson (2015), Geology, sulfide geochemistry
773 and supercritical venting at the Beebe Hydrothermal Vent Field, Cayman Trough. *Geochemistry,*
774 *Geophysics, Geosystems*, 16. <http://doi.org/10.1002/2015GC005879>

778 **FIGURE CAPTIONS**

779

780 **Figure 1:** **A:** Location and geological setting of the Mid-Cayman Spreading Centre (MCSC). **B:** 50 m-
781 gridded ship board multibeam bathymetry of the Mid-Cayman Spreading Centre showing the location of
782 Mt. Dent and the other major morphotectonic features discussed in the text: AVR = axial volcanic ridge, FZ
783 = fracture zone. Mt. Emms and Mt. Hudson were named in Cheadle et al. (2012) and are also OCCs on the
784 inside corners of the MCSC intersection with the adjacent fracture zones.

785

786 **Figure 2:** **A:** Map of MCSC showing the four different volcanic terrains. BVF and VDVF are the Beebe and
787 Von Damm Vent Fields; see Figure 1B for a colored version with bathymetric scale. Inset panels illustrate
788 the terrain types in more detail and using side-scan sonar to help identify each volcanic terrain type: **B:**
789 hummocky terrain, **C:** seamount, **D:** sheet flows.

790

791 **Figure 3:** **A:** Location map of the Southern segment, Central Basin and Horst. **B:** Shaded relief bathymetry
792 of the Horst with faulted regions labelled, based on high backscatter in TOBI data. **C:** Side-scan sonar
793 image of the Central Basin and Horst. Faults appear as brightly (acoustic) backscattering curvilinear
794 reflectors while sheet flows are smooth with moderate backscatter.

795

796 **Figure 4:** **A:** Location of the southern ridge-transform-intersection (RTI) between the MCSC and the Swan
797 Island fracture zone, inset box indicates location of panels C and D. Box B is the location of 3D image for
798 panel B. **B:** 3D projection (from the south) of a ‘lavafall’ formed by a sheet flow as it has cascaded over the
799 RTI fault scarp. The AUV bathymetry does not have the same depth color scale as the ship multibeam in
800 panels A and D. **C:** Side-scan sonar image with lava flows appearing as a strong reflector (bright) and
801 sediment covered areas with lower reflectivity. The RTI fault-scarp is a very bright curvilinear reflector.
802 Note the presence of a small high-standing ‘islands’ of sediment covered seafloor surrounded by brighter
803 sheet flows near to and NW of the RTI fault scarp, crossed by an ROV track (light orange). Also the area of
804 diffuse backscatter at the base, and SE of the RTI scarp. **D:** Geological map of the southern RTI showing
805 different volcanic terrains and faults.

806

807 **Figure 5:** **A:** 50 m resolution 3D bathymetric projection of Mt. Dent, looking northwest. The extent of the
808 AUV autosub6000 bathymetry survey is highlighted in white. Black box is the extent of Figure 6. Also
809 outlined in white dashes is the northern AVR, in black dashes are volcanoes, and in red lines are the
810 termination zone (squares on hanging wall) and normal faults (ticks on down-thrown side). **B:** 2 m-gridded
811 resolution AUV bathymetry of the domed surface of Mt. Dent, viewed from the south. Note that the AUV
812 and ship bathymetry have different scales. **C:** Rose diagram of corrugation orientations.

813

814 **Figure 6:** AUV-derived maps of the lower eastern flank of Mt. Dent. **A:** 1 m resolution, shaded relief
815 bathymetry. Lower red box the extent of Figure 8. **B:** 1 m-gridded multibeam backscatter, lighter is stronger
816 acoustic reflectivity. Upper red box indicates extent of Figure 7. **C:** Color-coded slope azimuth map
817 calculated from the 1 m-gridded bathymetry using a 3x3 matrix. **D:** Geological interpretation of the
818 termination zone. The dashed blue line is the curvilinear scarp with high backscatter that is interpreted here
819 as marking the trace of the termination zone.

820

821 **Figure 7:** 3D projected AUV-derived multibeam acoustic backscatter of the chaotic region north of where
822 the detachment trace bifurcates, see figure 6 and georeferenced tick-marks for location. Consolidated rafts
823 of lower-backscatter (sediment covered) seafloor surrounded by brighter areas of seafloor indicating freshly
824 exposed harder substrate (slumps) are annotated as a slump block.

825

826 **Figure 8:** Oblique image of the AUV data illustrating corrugations that characterize the lower eastern
827 flank of Mt. Dent. See Figure 6A and georeferenced tickmarks for location. See text for discussions of

828 the “Ghost Corrugations” observable to the east (above) the termination zone and arcuate structures
829 thought to be fault-related detritus accumulated along the corrugations.

830 **Figure 10:** **A:** Location map of panels B, on the crest of Mt Dent. **B:** The crest of Mt Dent showing N-S and
831 E-W orientated faults scarps (white lines) form grabens which produce basins. Pockmarks (blue
832 dots) identified from AUV bathymetry (C). **C:** Zoom in of box C in panel B showing pockmarks in
833 bathymetry as circular depressions. **D:** photograph from the ROV HyBIS of a pockmark from within the
834 pock-mark field located as the yellow ‘X’ in panel B.

835

836 **Figure 11:** Schematic block diagram illustrating the key elements of the dying stages of the Mt. Dent OCC.
837 The OCC is formed by detachment faulting, emerging from the termination zone and aging to the west,
838 exposing a foot wall that has corrugations parallel to the detachment fault’s slip direction, and a
839 heterogeneous ‘plum-pudding’ crustal structure comprising gabbroic plutons and dikes intruded into a
840 matrix of serpentinitised ultramafic mantle material. The northern AVR intersects Mt Dent’s northern flank,
841 while in the south, the horst cuts obliquely into Mt Dent’s southern flank. The hanging wall immediately to
842 the east and above the detachment fault comprises recent volcanics, including a seamount. Subtle
843 ornamentation depicts hypothesized magmatic intrusions under the VDVF and the detachment (red) and
844 associated fluid flow (blue).

845

846

847

848

849

850

Figure 1.

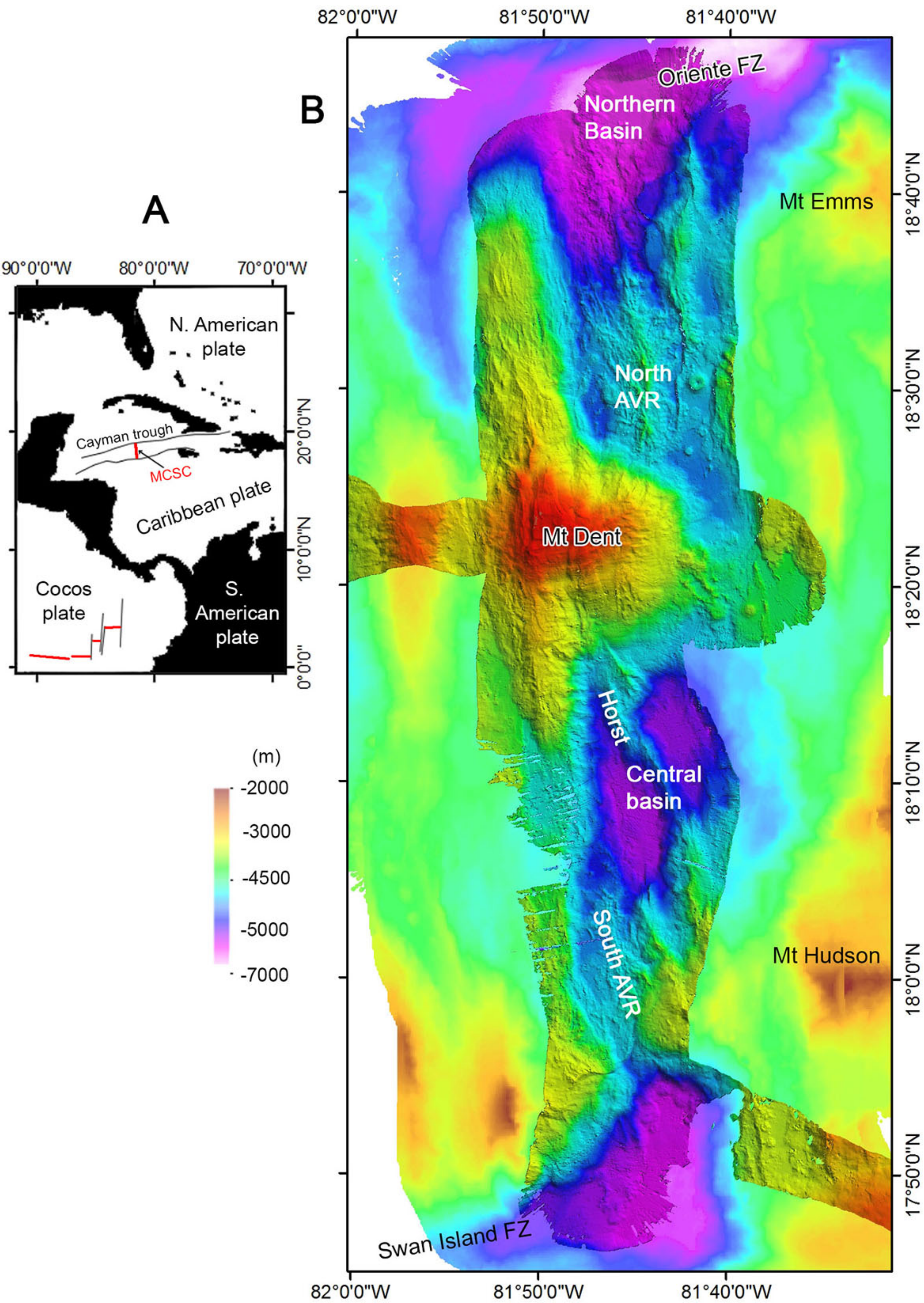
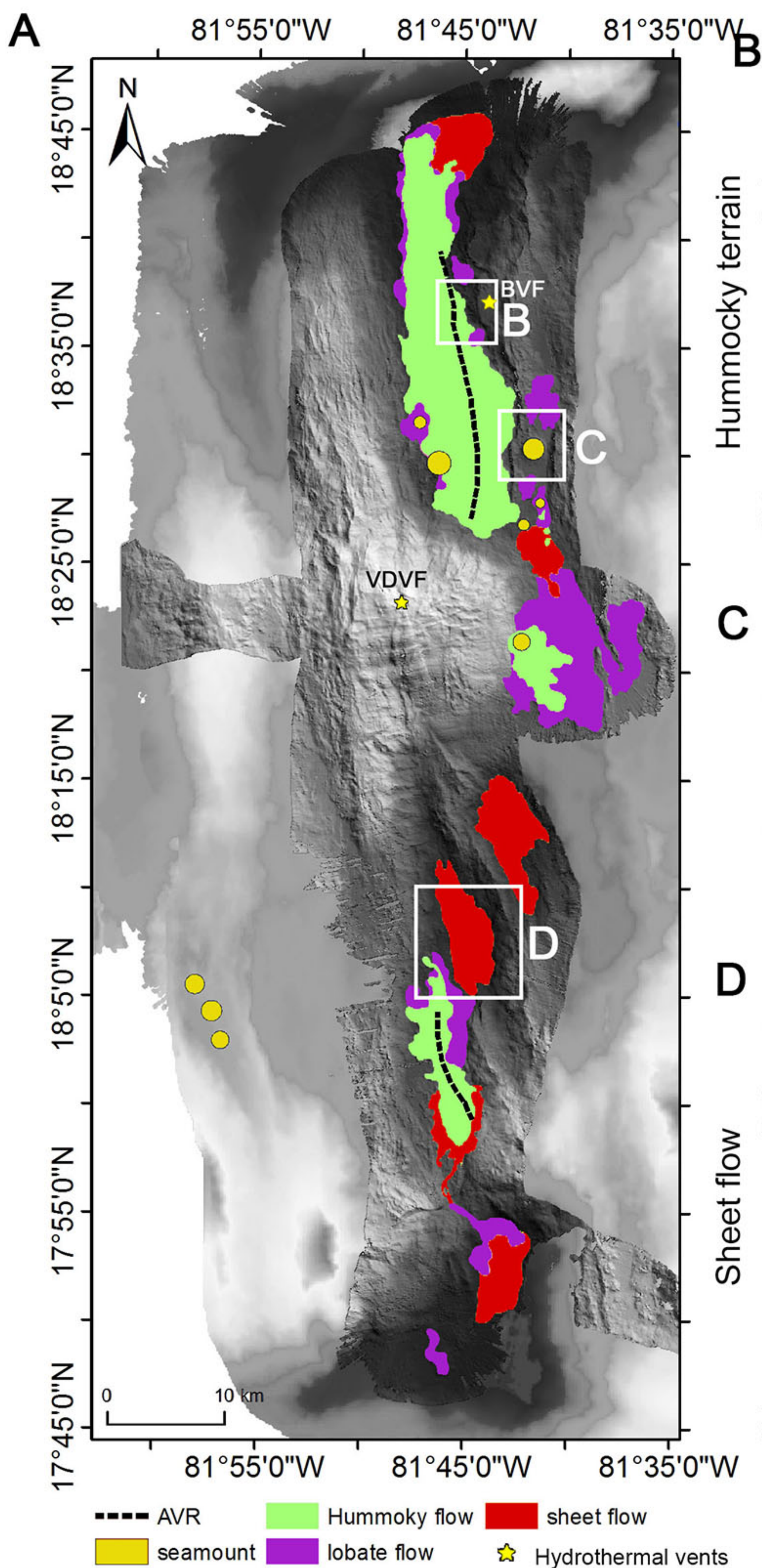


Figure 2.



B Hummoky terrain
C Seamount
D Sheet flow

Bathymetry

Side-scan sonar

Seamount

Bathymetry

Side scan sonar

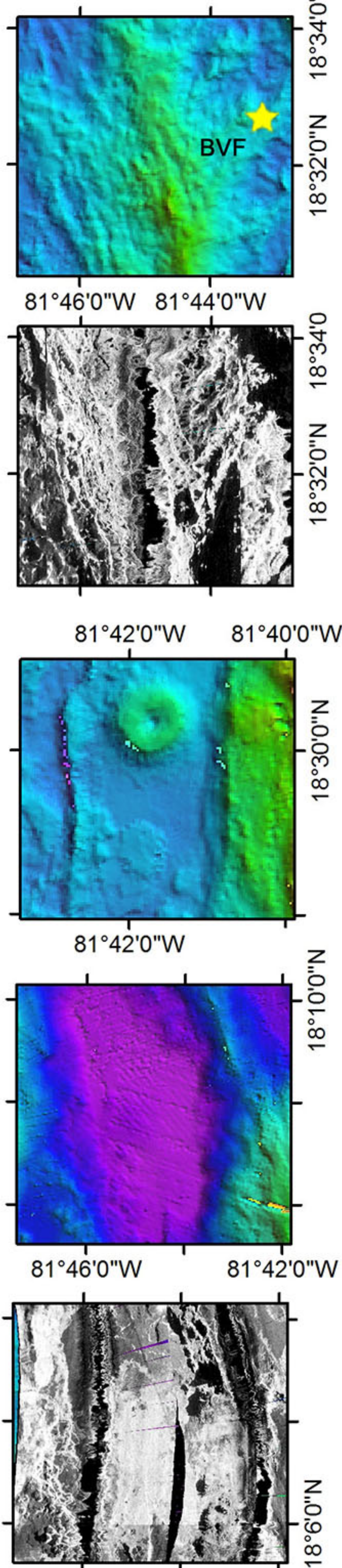
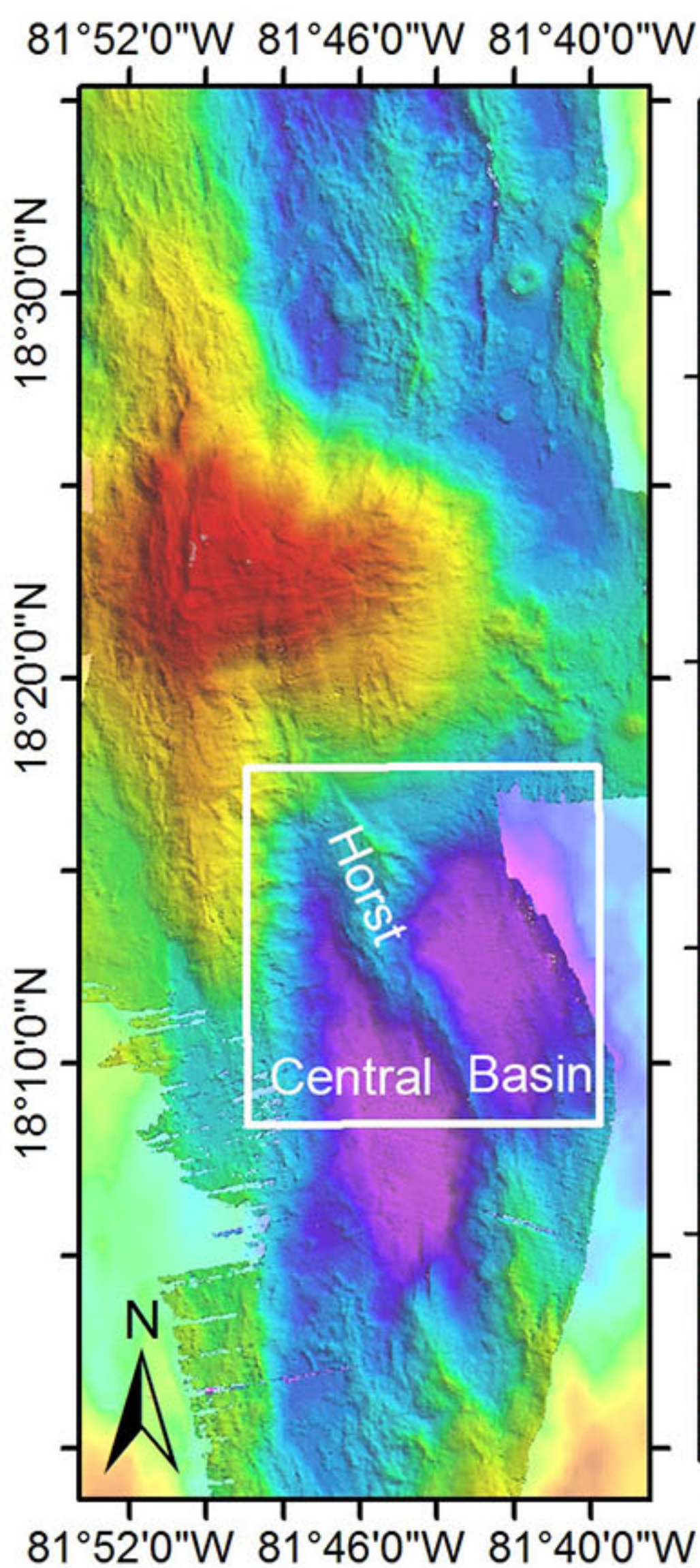
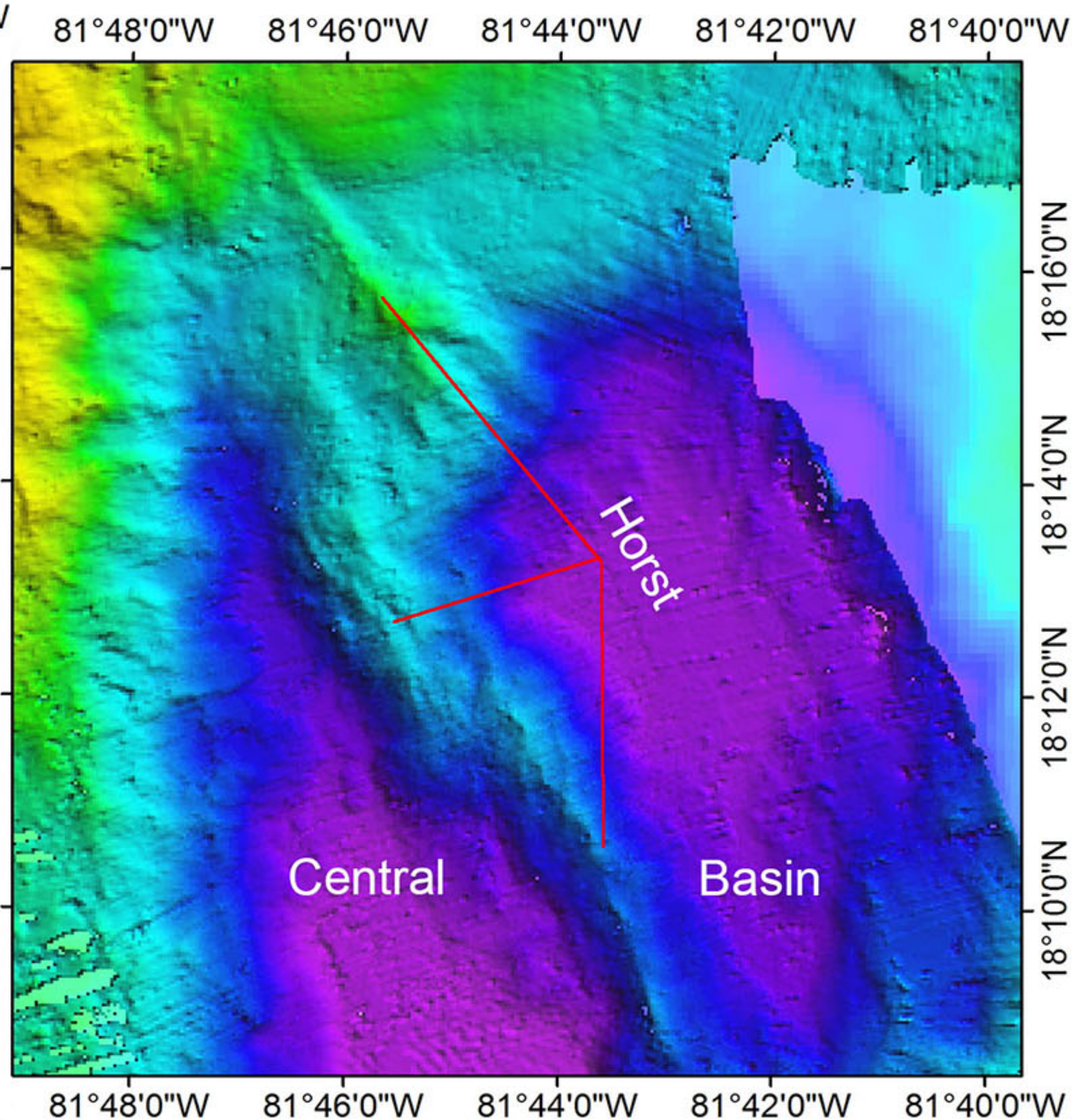


Figure 3.

A**B****C**

Bathymetry
(m)

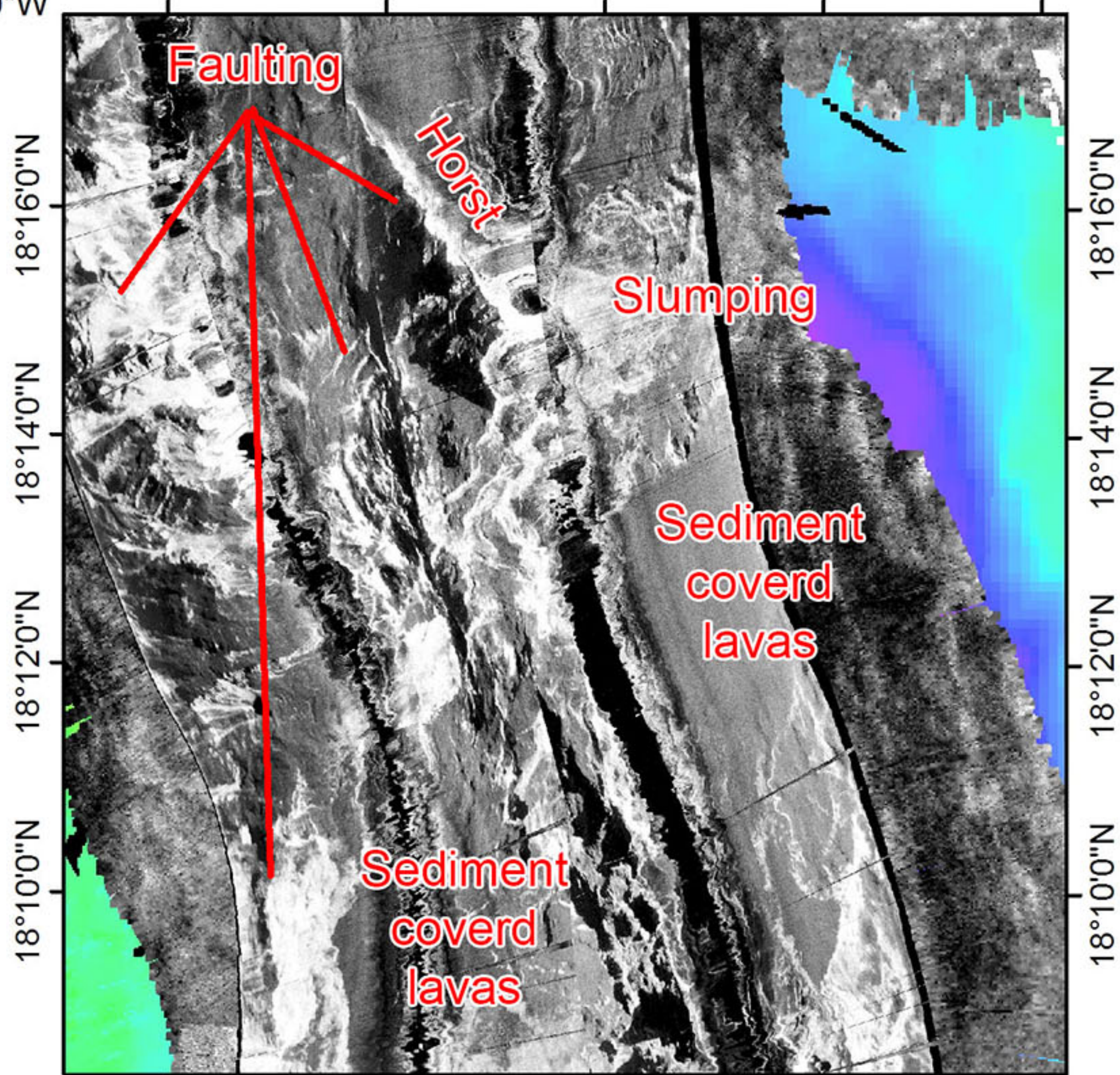
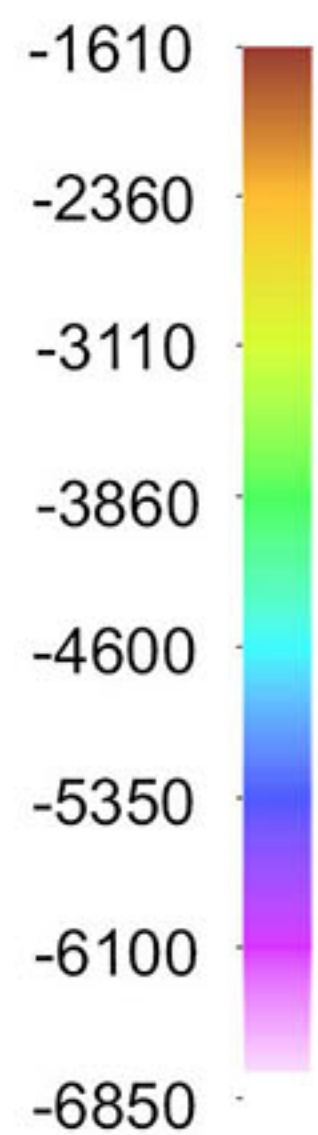


Figure 4.

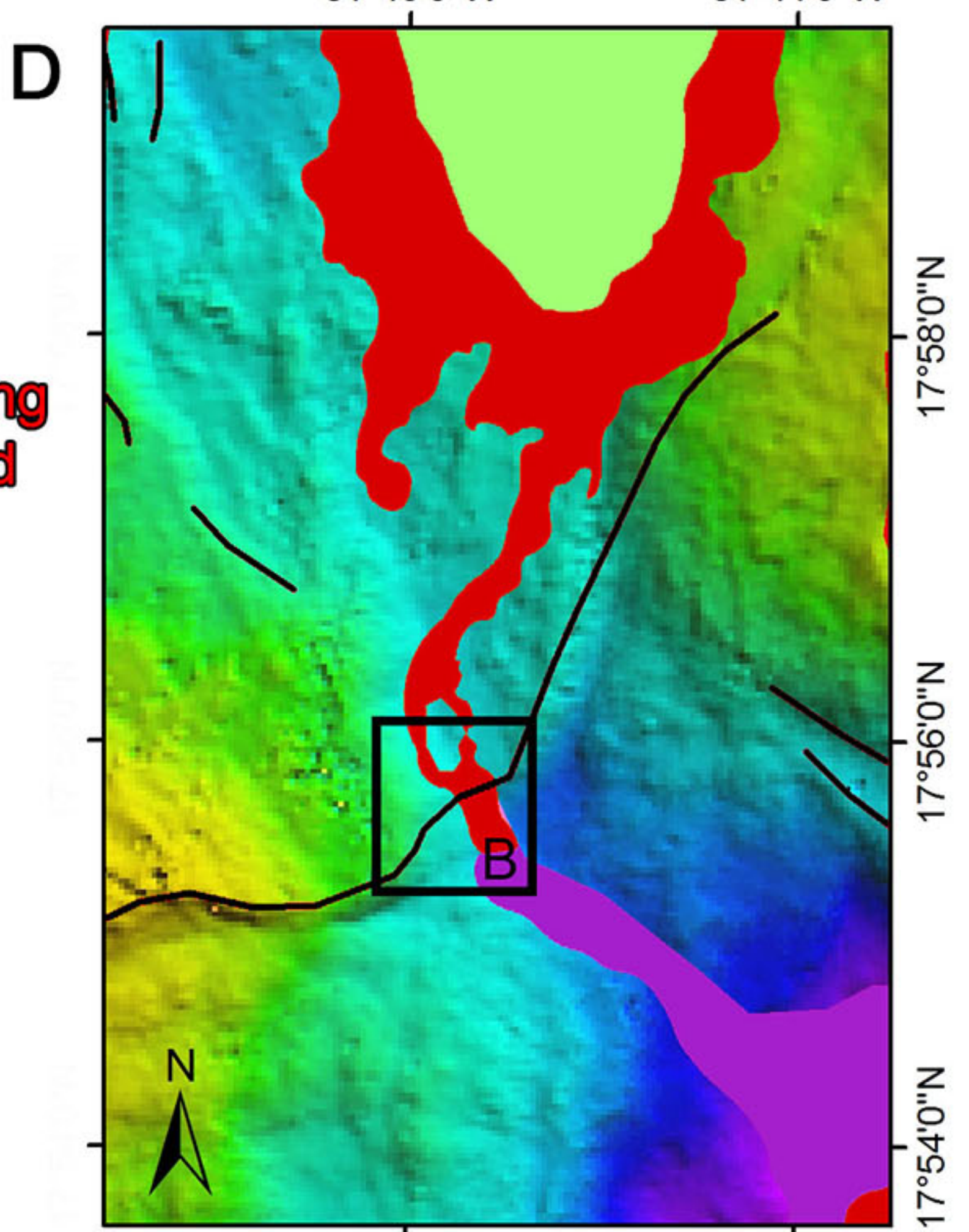
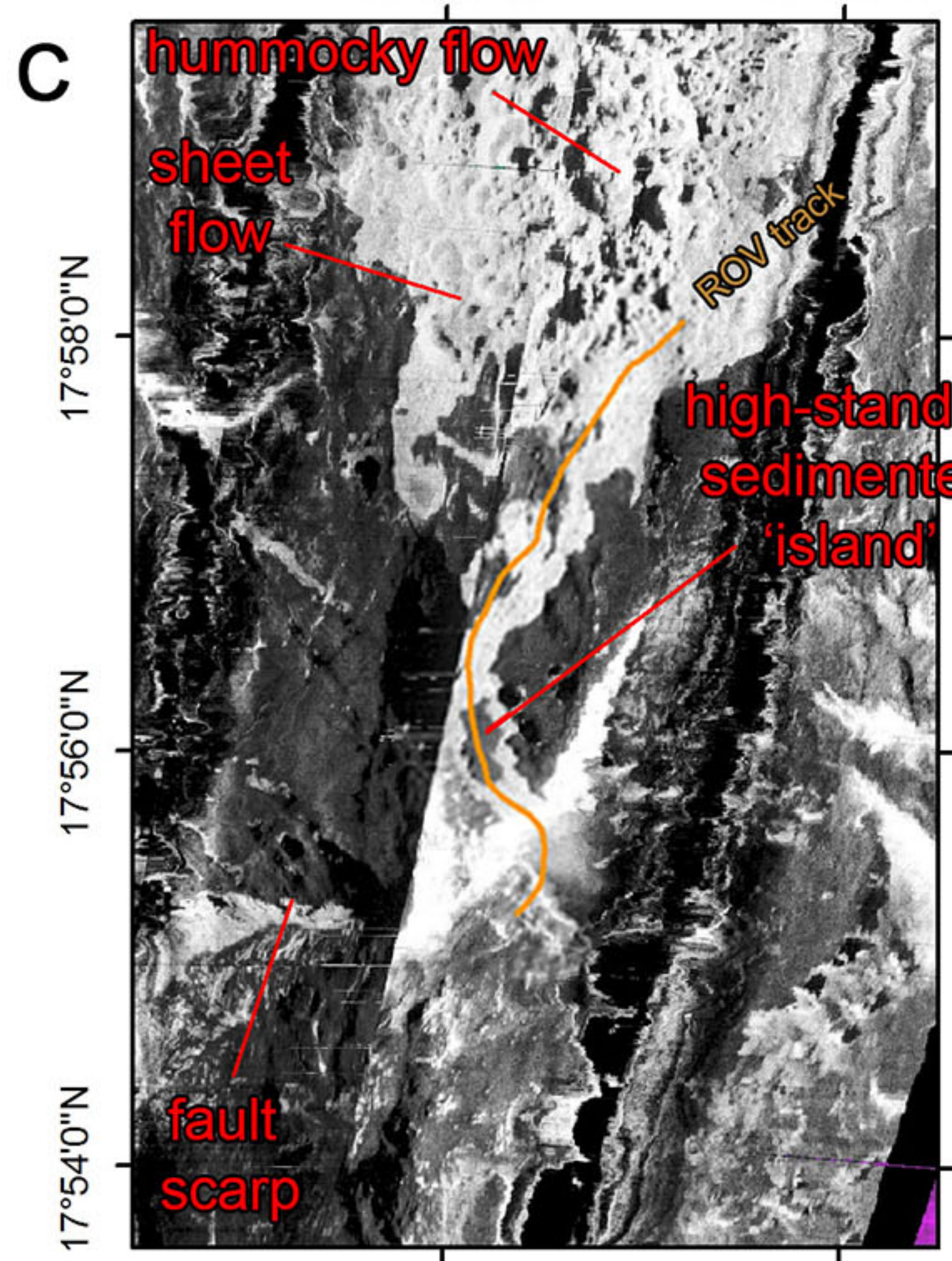
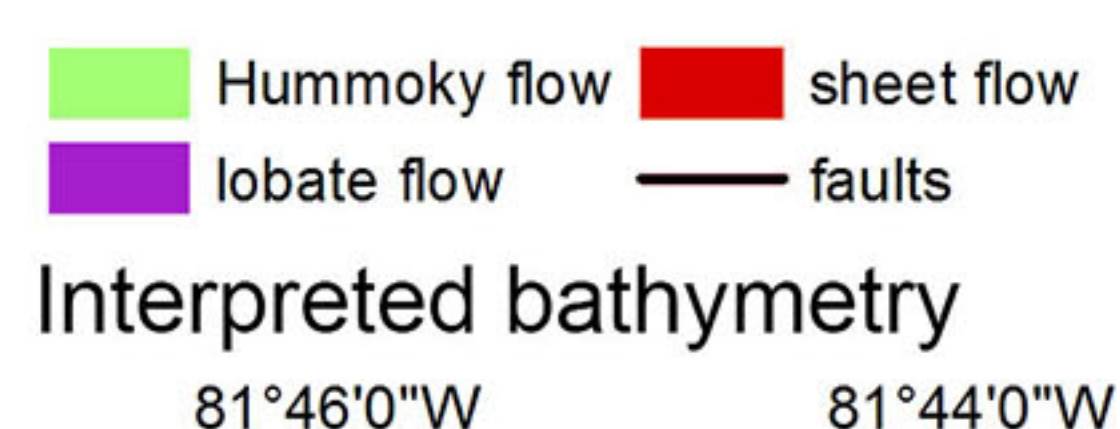
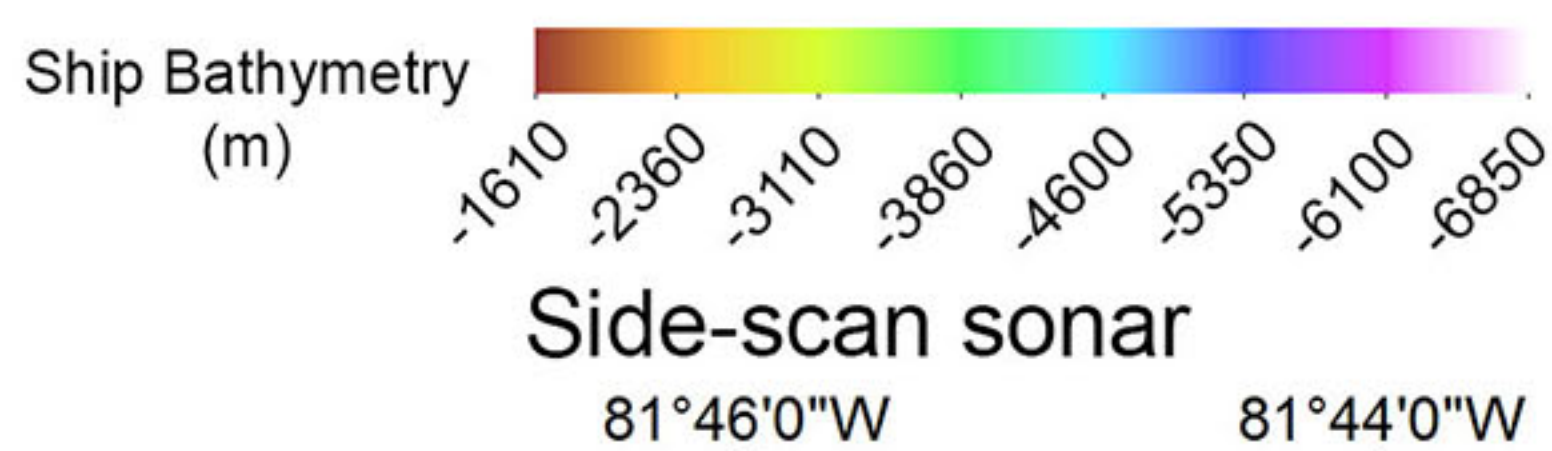
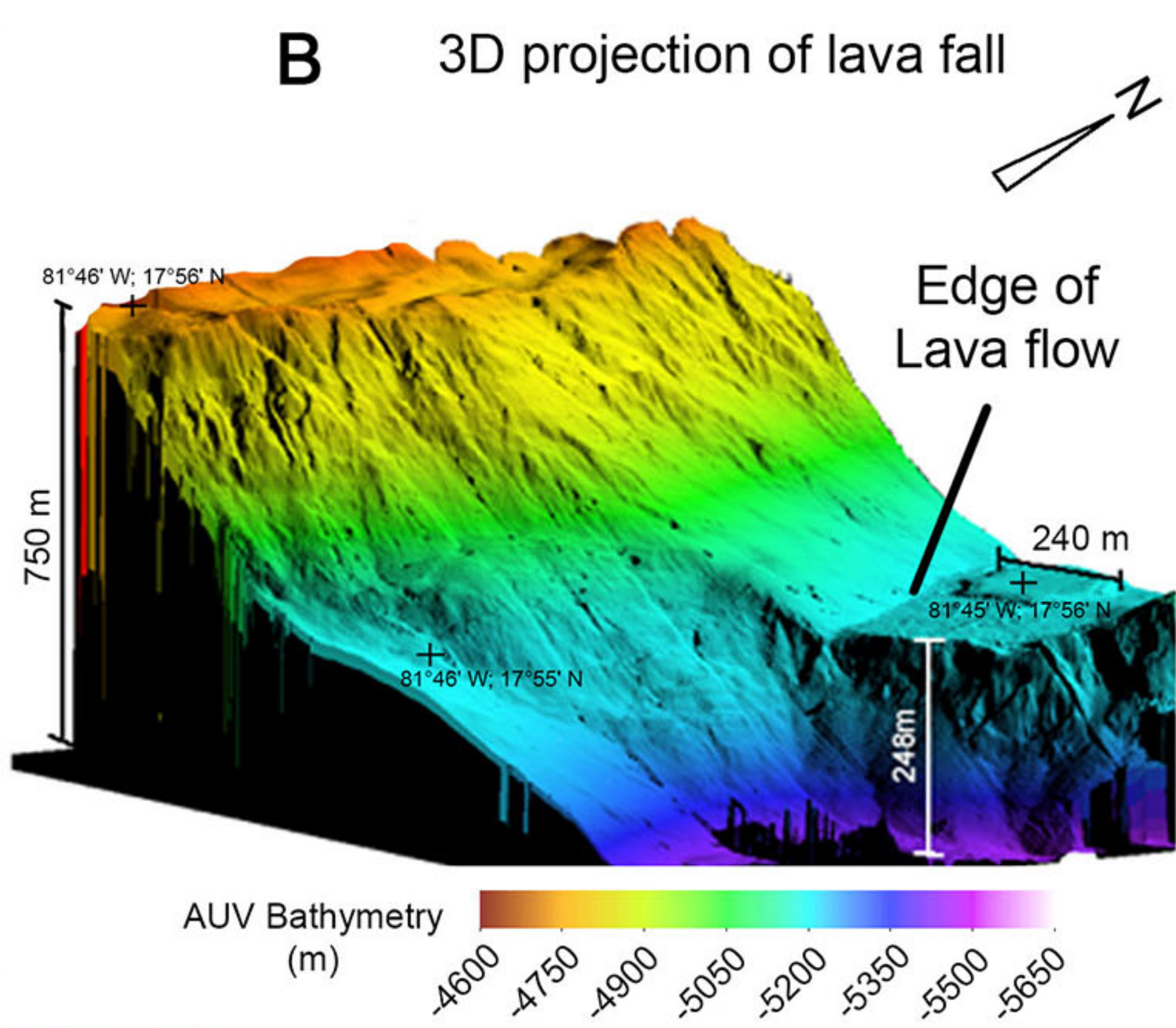
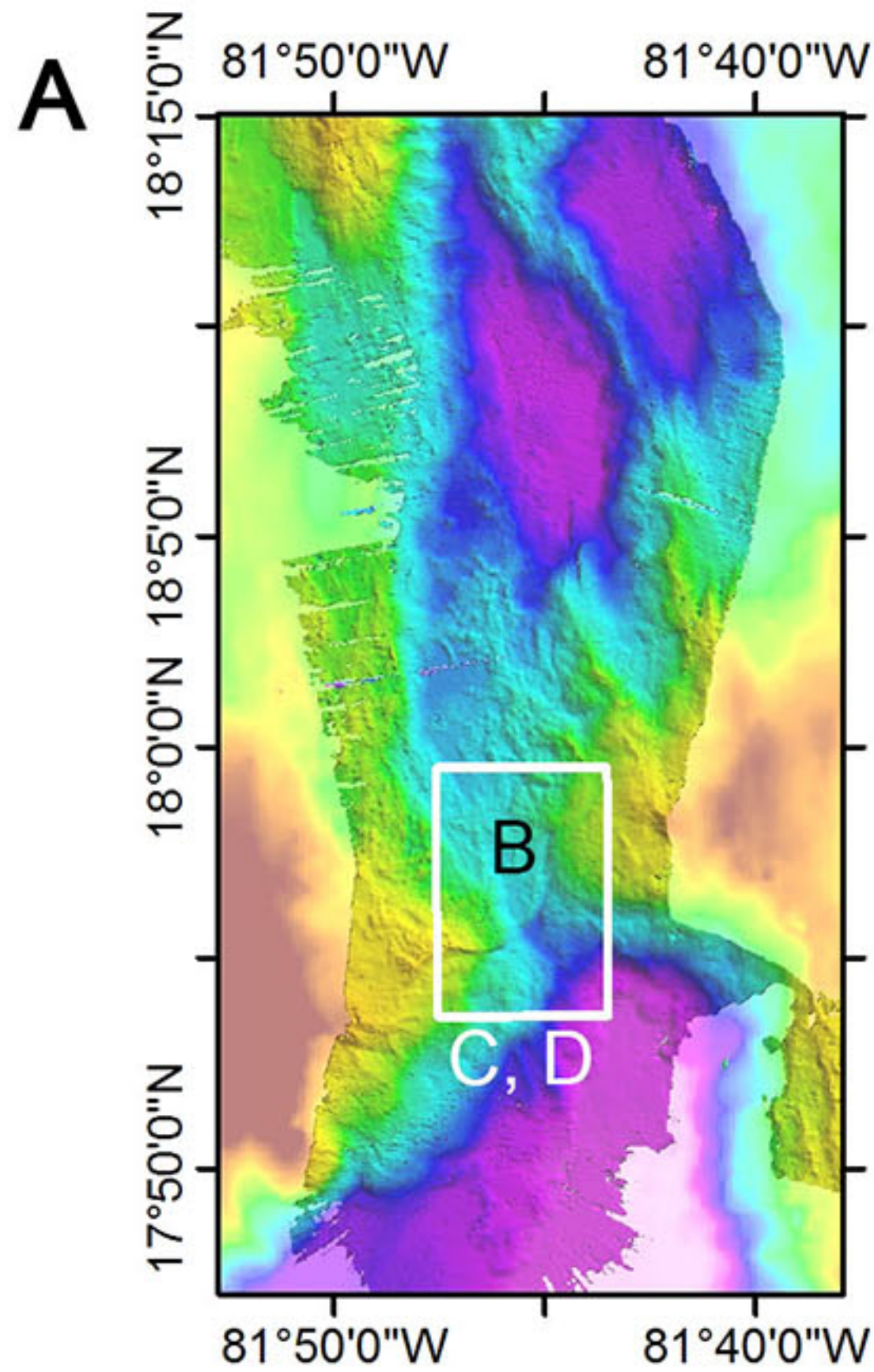
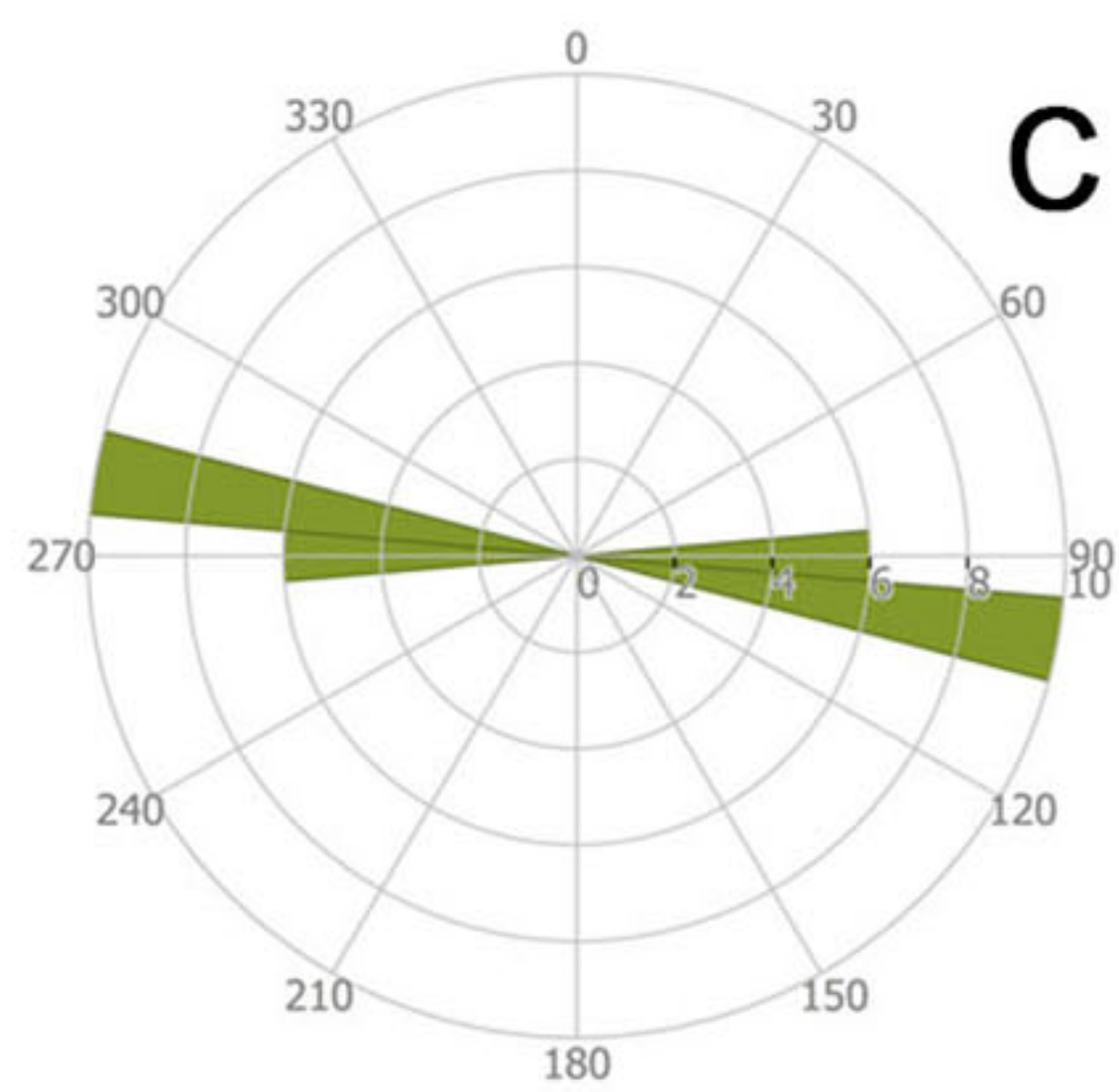
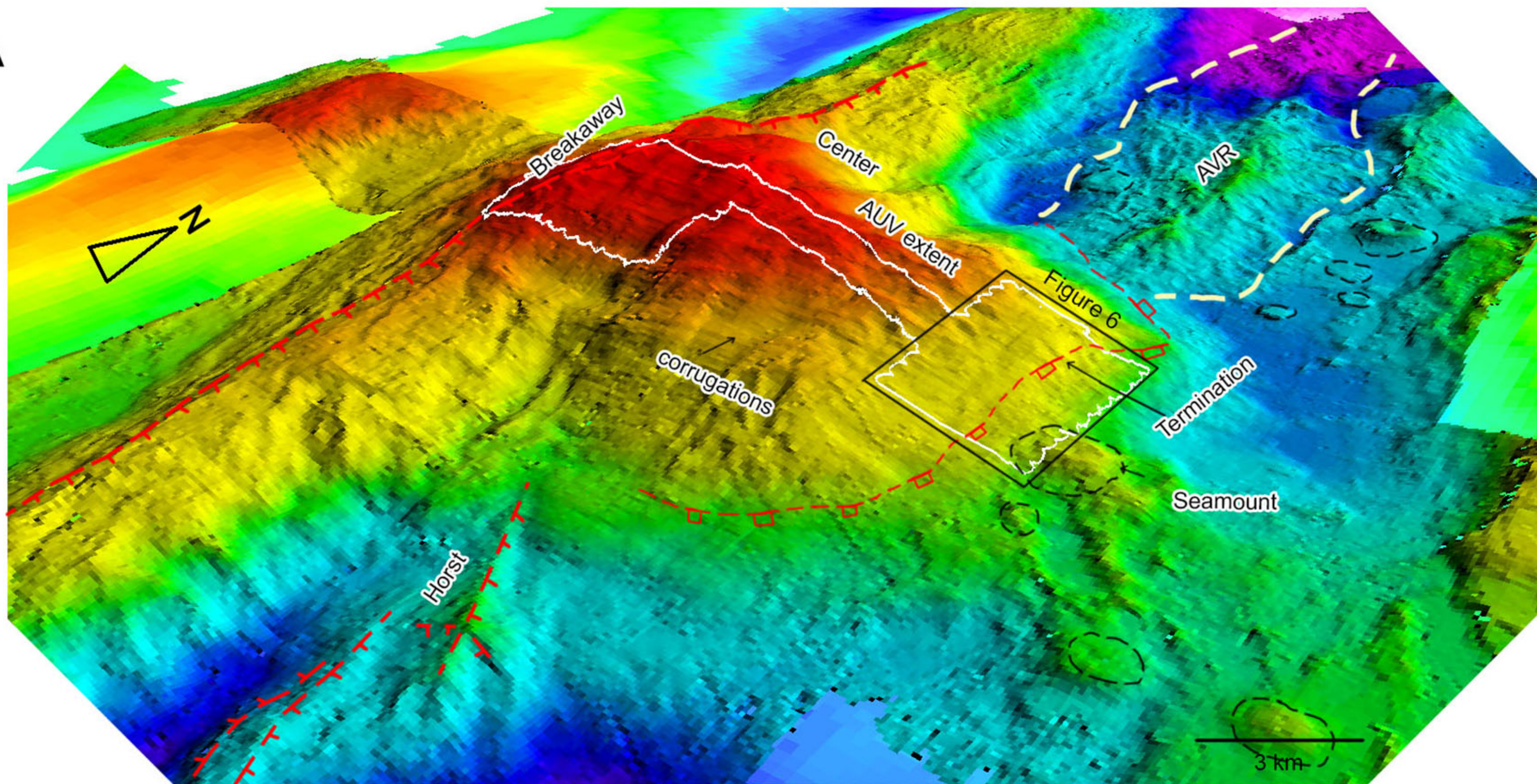


Figure 5.

A

Ship Bathymetry (m)

AUV Bathymetry (m)

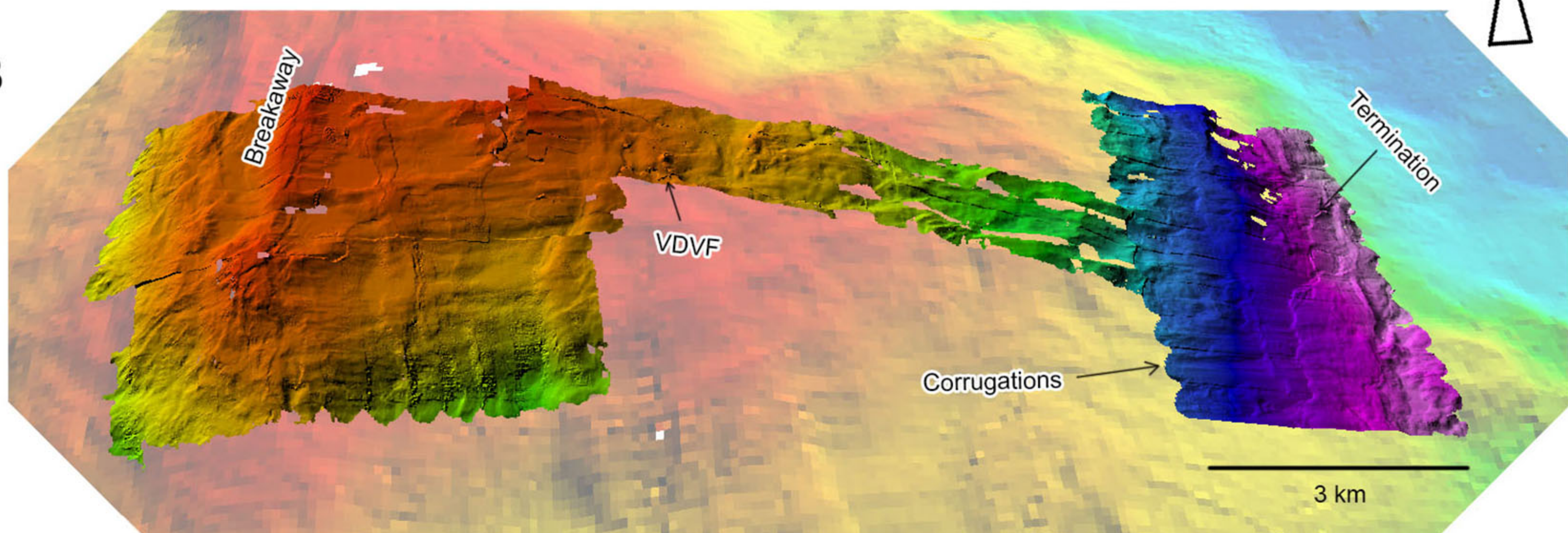
B

Figure 6.

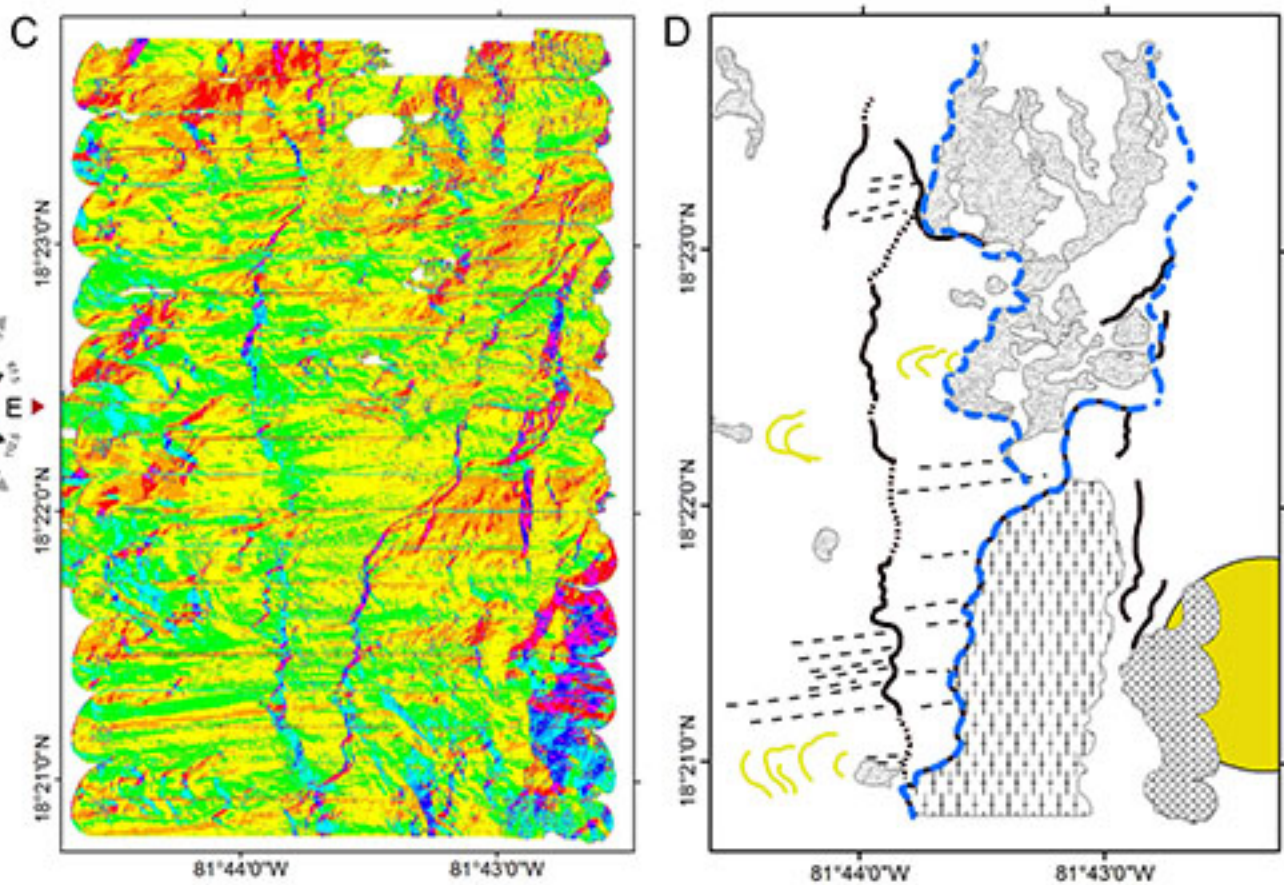
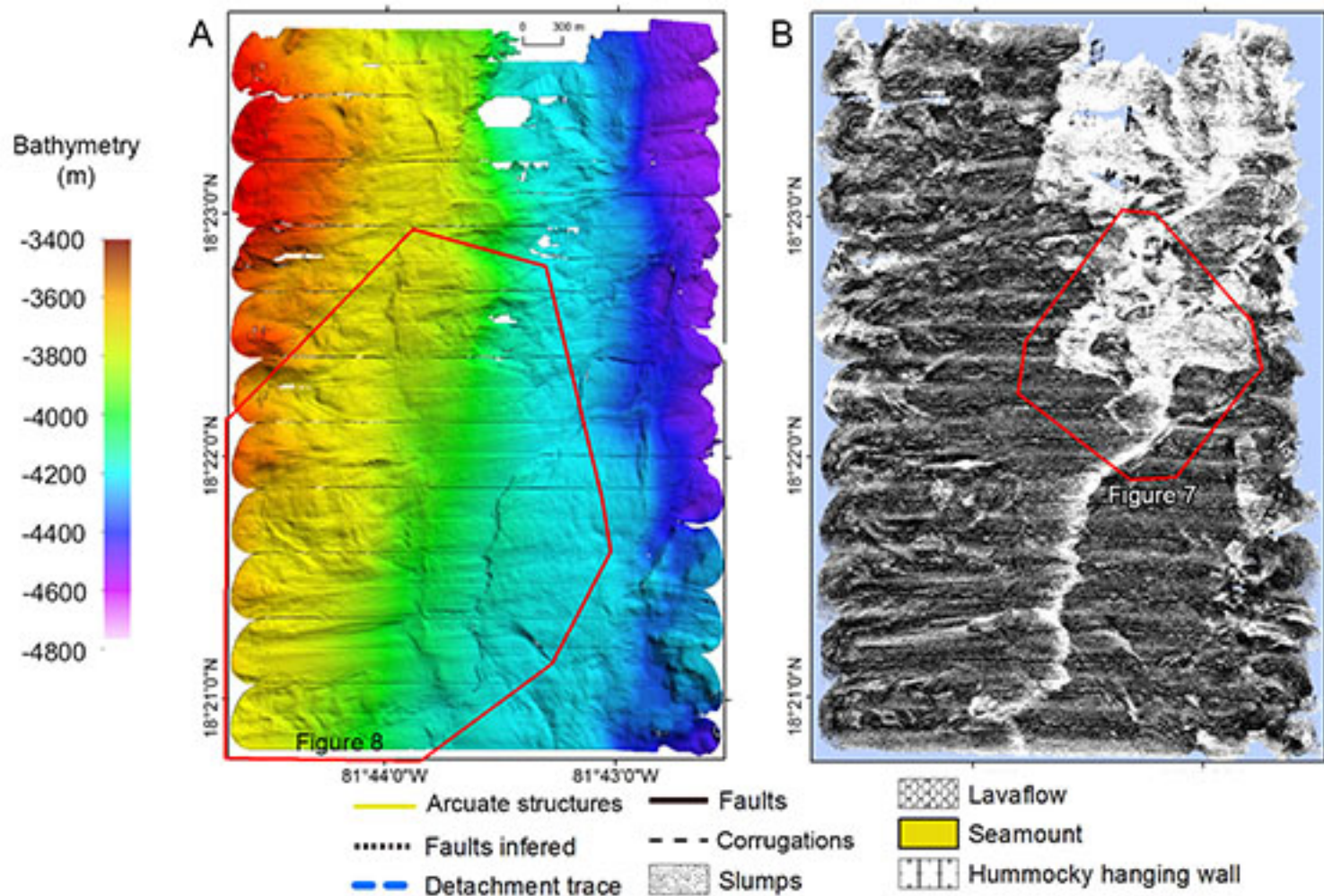


Figure 7.

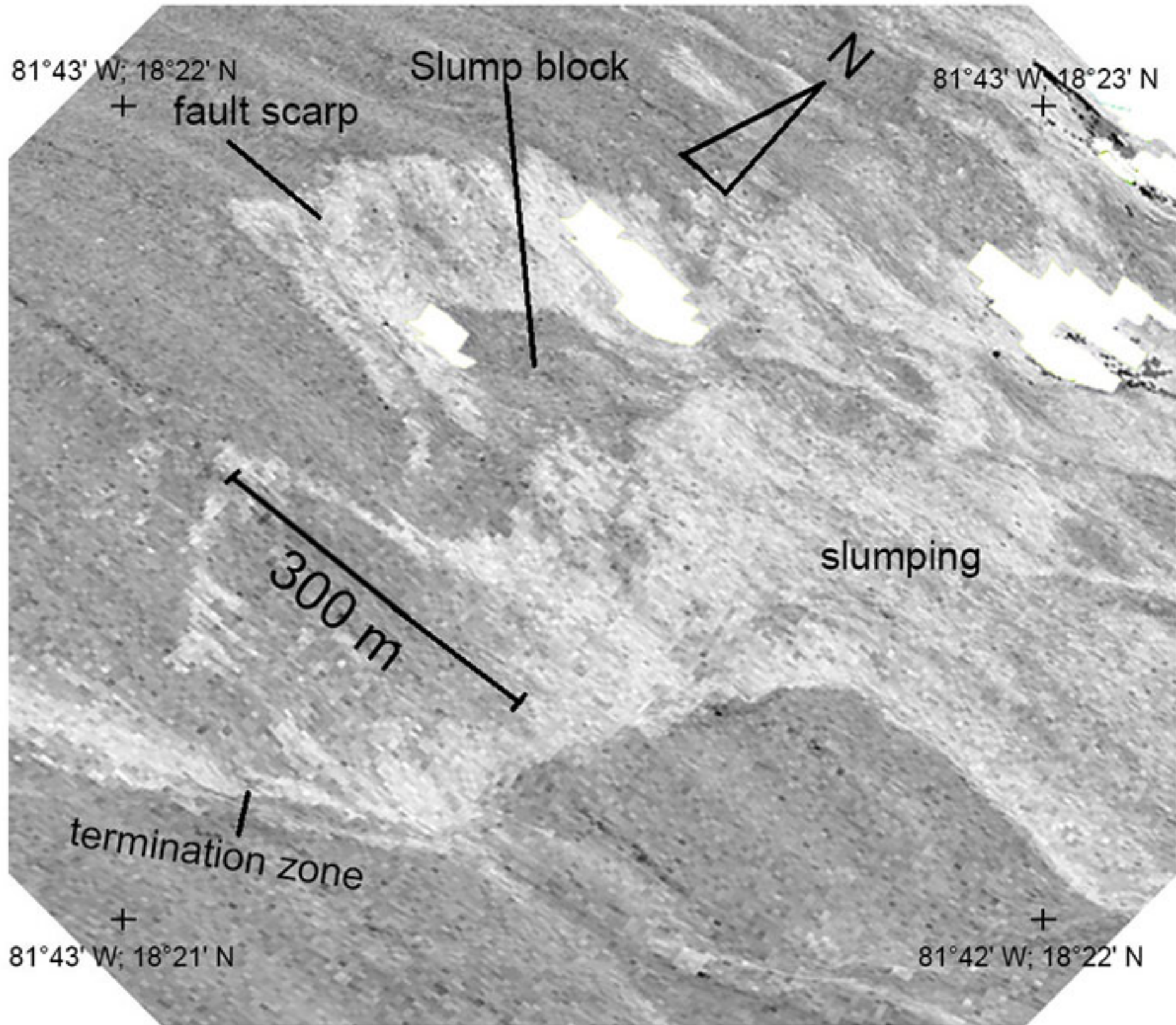


Figure 8.

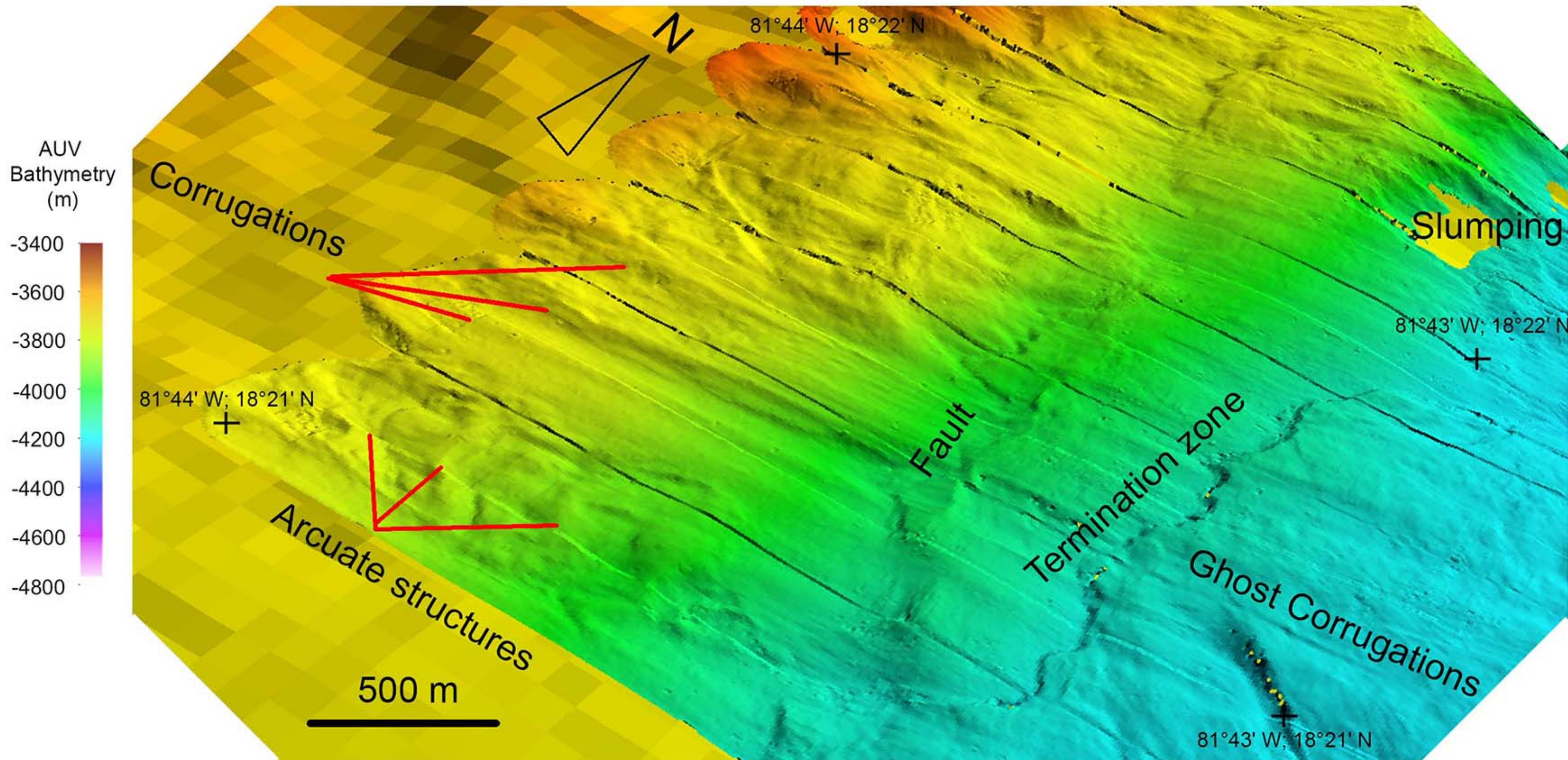


Figure 9.

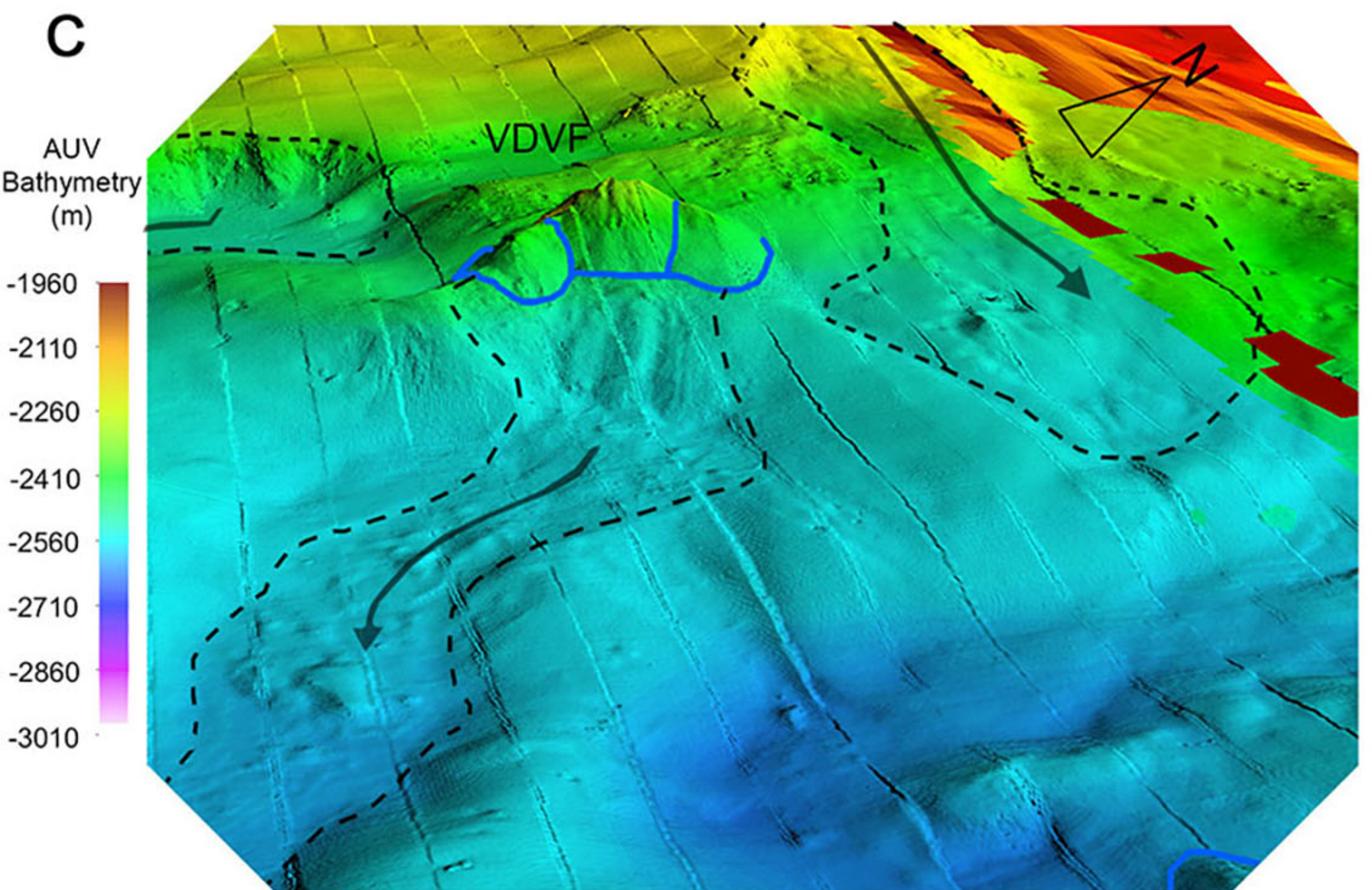
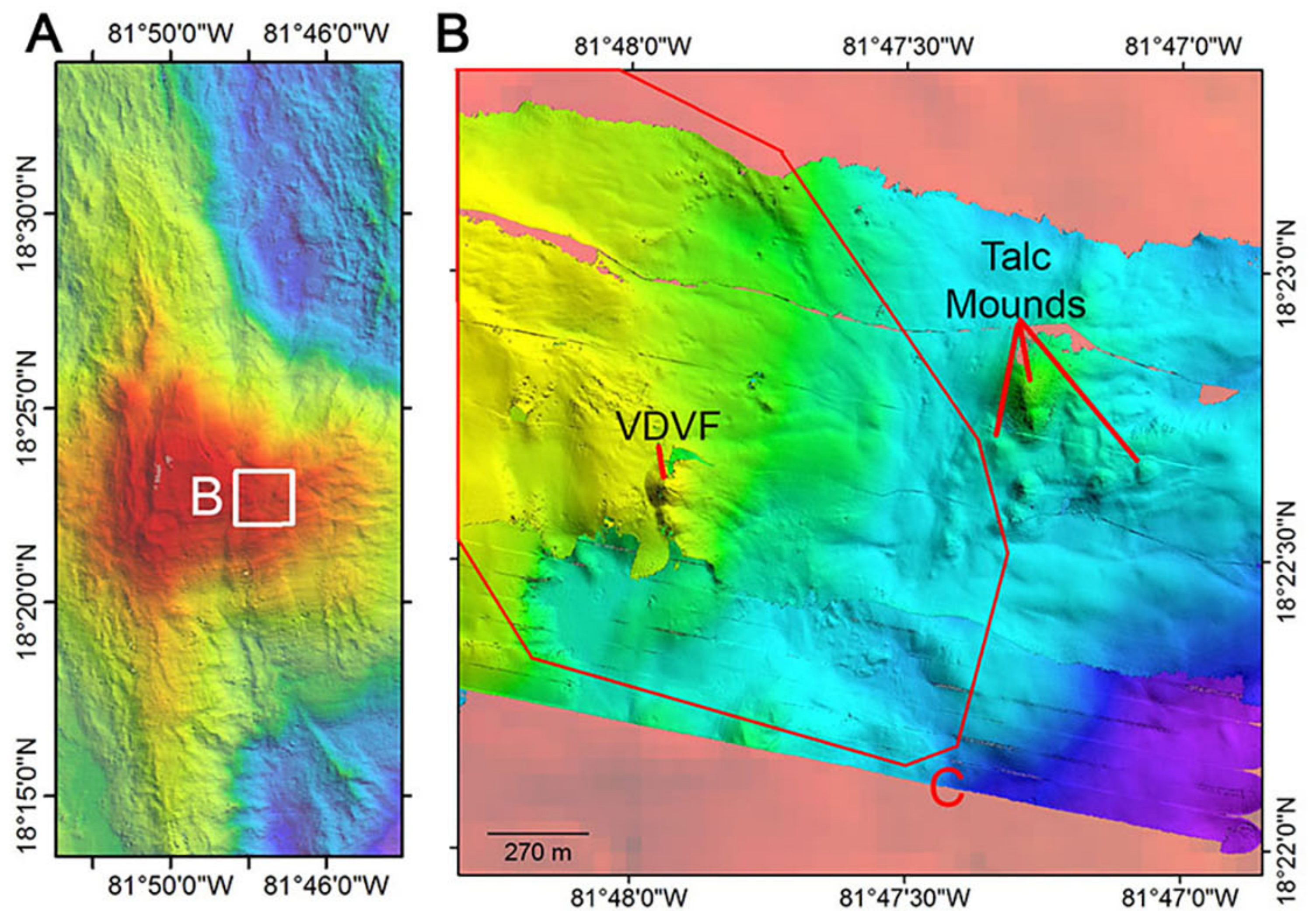


Figure 10.

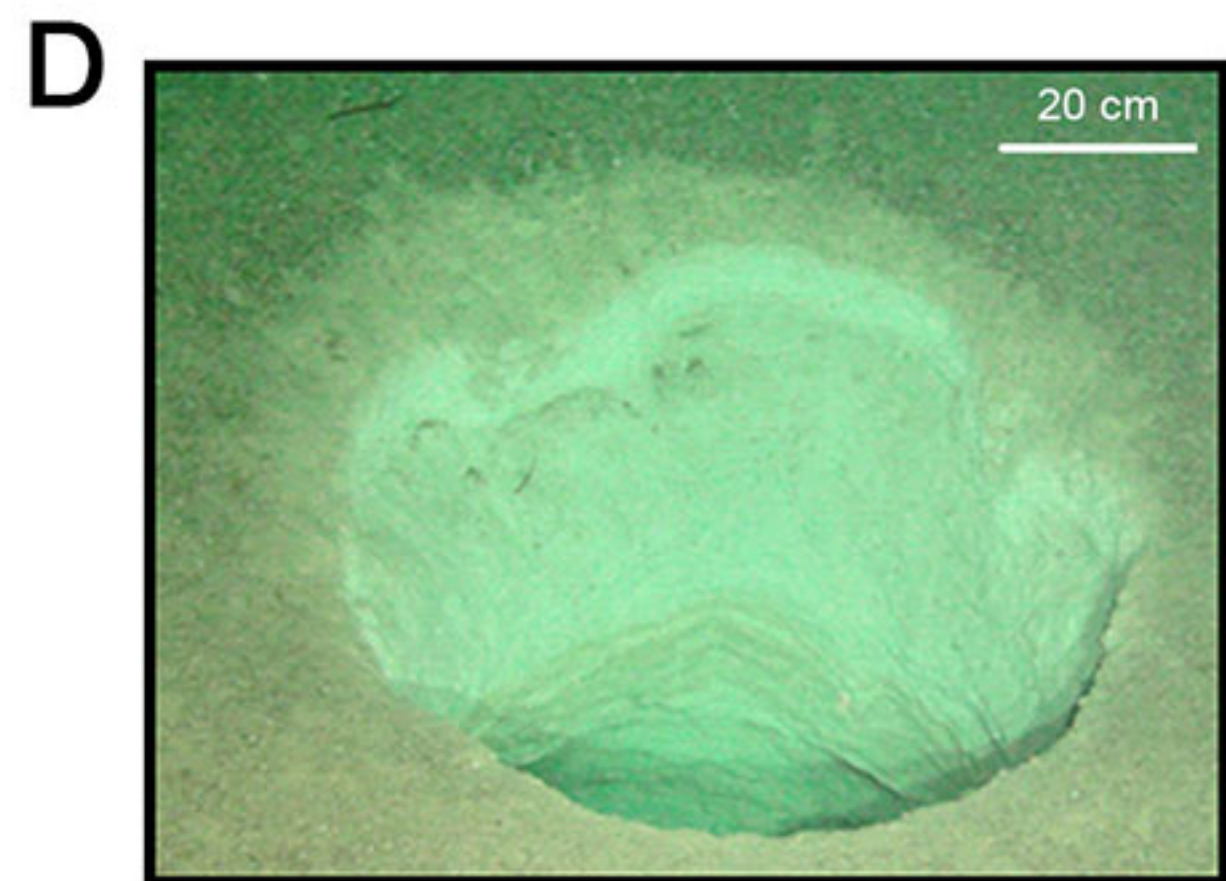
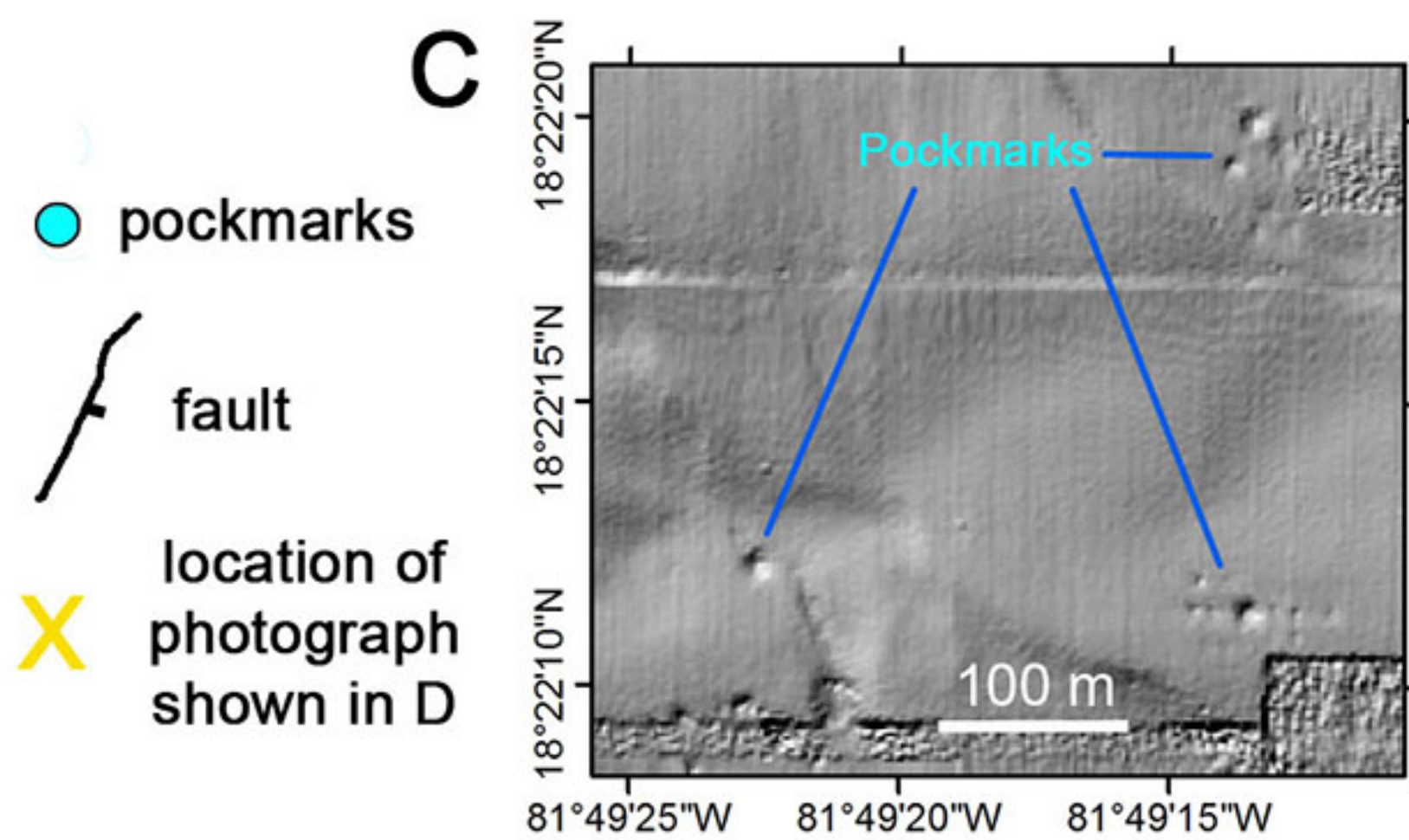
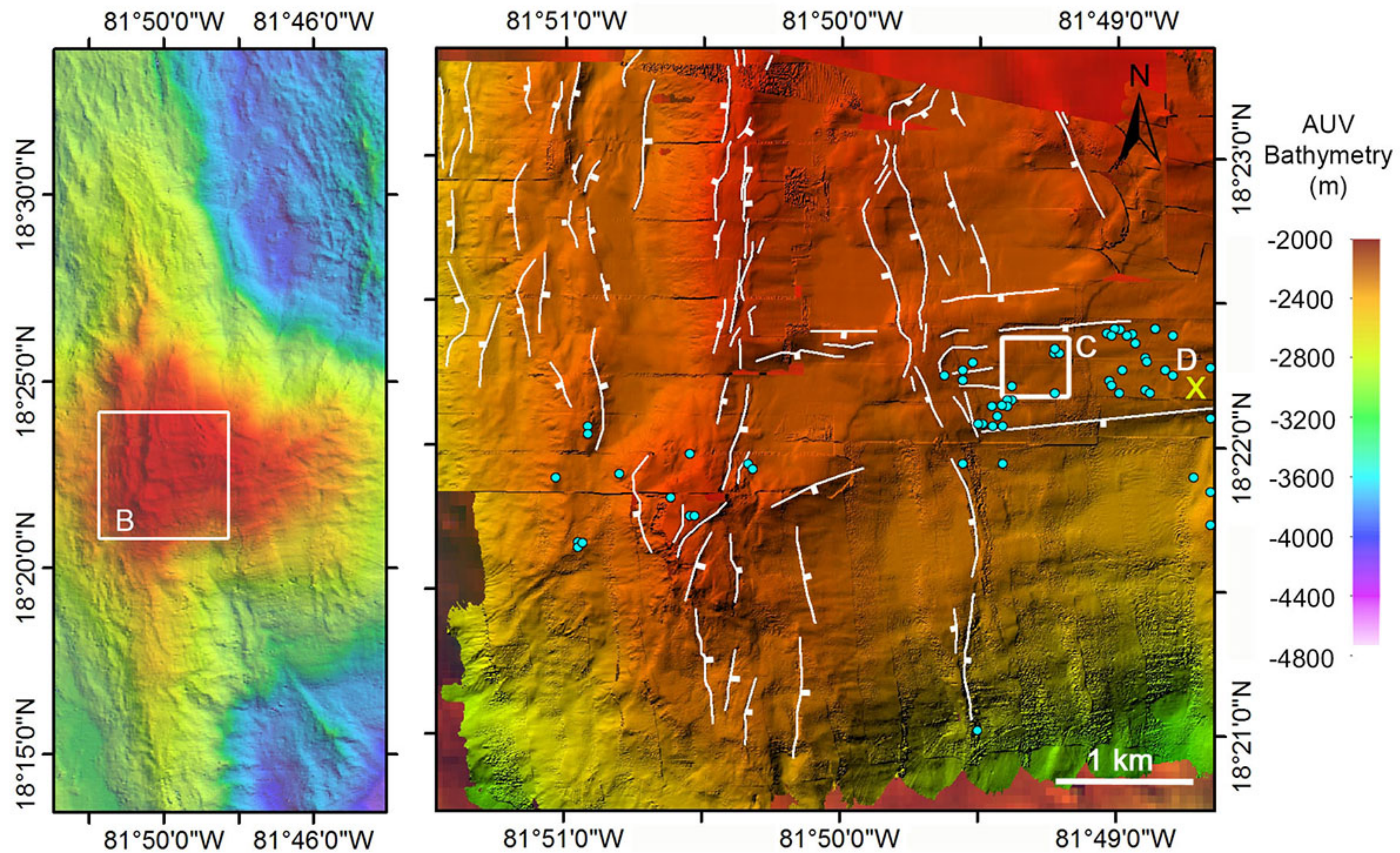


Figure 11.

